Published version available at: https://www.sciencedirect.com/science/article/pii/S0263822321009612
DOI: https://doi.org/10.1016/j.compstruct.2021.114499

High-fidelity analysis of multilayered shells with cut-outs via the discontinuous Galerkin method

Giuliano Guarino[a], Vincenzo Gulizzi[b], Alberto Milazzo[a,*]

[a]*Department of Engineering, Università degli Studi di Palermo, 90128, Italy*
[b]*Center for Computational Sciences and Engineering (CCSE), Lawrence Berkeley National Laboratory MS 50A-3111, Berkeley, CA 94720, USA*

Abstract

A novel numerical method for the analysis of multilayered shells with cut-outs is presented. In the proposed approach, the shell geometry is represented via either analytical functions or NURBS parametrizations, while generally-shaped cut-outs are defined implicitly within the shell modelling domain via a level set function. The multilayered shell problem is addressed via the Equivalent-Single-Layer approach whereby high-order polynomial functions are employed to approximate the covariant components of the displacement field throughout the shell thickness. The shell governing equations are then derived from the Principle of Virtual Displacements of three-dimensional elasticity and solved via an Interior Penalty discontinuous Galerkin method over a discretization of the shell modelling domain that is obtained by intersecting a background structured grid with the level set function defining the cut-outs. To maintain high-order accuracy even in proximity of the embedded cut-outs, high-order accurate quadrature rules for implicitly-defined regions are employed to compute the integrals of the method while a cell-merging technique avoids the presence of overly small cut cells. The combined use of these features represents the novelty of the proposed method and provides a high-fidelity approach to the analysis of multilayered shells with cut-outs. Numerical tests are performed to model the static response of a cylindrical shell and a NURBS-based shell with a cut-out. The obtained results are compared with those obtained using the Finite Element method and show the accuracy and the computational efficiency of method.

Keywords: Multilayered shells; Cut-outs; Interior Penalty discontinuous Galerkin; High-order modeling; NURBS; Implicit mesh

1. Introduction

In advanced industrial applications where weight minimization is required, multilayered composite structures are typically the preferred structural choice as the designer can take advantage of different optimization strategies involving, for example, the selection of the fibers and the matrix materials, the fibers' volume fraction and the stacking sequence [1, 2]. However, in several cases, the design of composite structures must

*Corresponding author
Email addresses: giuliano.guarino@unipa.it (Giuliano Guarino), vgulizzi@lbl.gov (Vincenzo Gulizzi), alberto.milazzo@unipa.it (Alberto Milazzo)

comply with non-structural specifications, such as the curved geometry dictated by the aerodynamics requirements in the aerospace industry, and/or must account for the presence of embedded cut-outs, which are needed for installation and inspection of other components. In such configurations, the use of high-fidelity computational tools is necessary to resolve the complex distribution of the mechanical fields induced by the curvature, the material heterogeneity and the regions of stress concentration.

The shell problem is in general a fully three-dimensional (3D) problem requiring fully 3D numerical models; however, 3D models easily become overly demanding in terms of computational resources. As an alternative, researchers have introduced the so-called two-dimensional (2D) theories, which are based on specific assumptions on the behavior of the variables of interests throughout the thickness of the considered structure and allow reducing the computational costs of the associated numerical models. In the literature, it is possible to distinguish between the Equivalent Single Layer (ESL) theories and the Layer-Wise (LW) theories. In ESL theories, see e.g. [3–5], the functions used to expand the displacement field along the thickness are defined uniquely and are valid for each layer of the multilayered shells; on the other hand, the Layer-Wise (LW) theories are based on a layer-by-layer expansion so that the displacement field is described by piecewise functions that at the layers interfaces have only a C_0 continuity [6–8]. The variety of theories that fall in these two categories lead to many formulations, which have been elegantly treated in a unified fashion by Carrera [9, 10] via the so-called Carrera Unified Formulation (CUF).

Similarly to the case of three-dimensional elasticity, the solution of the governing equations of shell theories requires numerical methods because analytical or semi-analytical techniques are limited to very few specific combinations of geometry, materials and boundary conditions as shown, for instance, in Refs.[11–13]. Among the computational approaches available in the literature, the Finite Element Method (FEM) has been used extensively in industry and it is still an active research area [14, 15]. Several alternative approaches have also been proposed, among which, the Generalized Differential Quadrature [16, 17], the Ritz method [18–20], the Isogeometric Analysis approach [21] are worth mentioning.

The discontinuous Galerkin (dG) method has also gained recent interest for applications involving elliptic equations [22–24], including those governing the behavior of plates and shells [25–27]. In the dG method the variables of interest are approximated by polynomials that are discontinuous at the elements interfaces, while the continuity among nearby elements and the boundary conditions are enforced in a weak sense through suitable integrals along the elements boundaries. This allows the dG method to be naturally amenable to the use of general high-order basis functions, generally-shaped mesh elements and domain discretizations with local h and p refinements.

In the context of high-order plates and shell theories, the dG method has been successfully employed for the solution of the governing equations of multilayered elastic plates modelled by ESL and LW theories [28, 29], to multilayered piezoelectric plates modelled by LW theories [30] and to multilayered shells modelled by ESL theories [31]. To account for the presence of cut-outs, in Refs.[28, 29], the authors combined an easy-to-generate background grid with an implicit representation of the cut-out geometry via a level set function;

however, their application was focused on multilayered plates.

The aim of this work is then to present an original high-fidelity numerical framework for the analysis of multilayered shells with cut-outs based on high-order shell theories and the discontinuous Galerkin method. The framework is termed high-fidelity because it allows the treatment of generally-curved multilayered shells with generally-shaped cut-outs and it provides a high-order resolution of the mechanical fields of interest throughout both shell thickness and the shell modelling domain. From the viewpoint of the geometry description, this is achieved by mapping the shell mid-surface via either user-defined analytic functions or NURBS parametrizations, which allows the coupling of the proposed scheme with modern computer-aided-design (CAD) software libraries, and by the use of a level set function to resolve the presence of cut-outs. From the viewpoint of the high-order solution of the multilayered shell problem, high-order polynomials functions are employed throughout both the shell thickness, following an ESL approach, and the shell modelling domain, where the governing equations are solved via an Interior Penalty dG method previously developed for multilayered plates and shells [28, 29, 31] and extended here to the analysis of multilayered shells with implicitly-defined cut-outs.

The article is organized as follows: Sec.(2) introduces the geometry description, the constitutive behavior and the ESL approximation, which are subsequently used to derive the governing equations of the 2D boundary-value problem for multilayered shells starting from the Principle of Virtual Displacements from three-dimensional elasticity; Sec.(3) recalls the Interior Penalty dG scheme for the solution of the governing equation derived in Sec.(2), while Sec.(4) discusses the details of the application of the dG method for domain discretizations with embedded cut-outs. In Sec.(5), the proposed method is employed to model the static response of a cylindrical shell and a NURBS-based shell with an implicitly-defined cut-out. Finally, Sec.(6) draws the conclusions and suggests some directions for further developments.

2. Boundary values problem

The considered generic multilayered shell consists of a stacking of N_ℓ homogeneous, orthotropic and perfectly-bonded layers. The ℓ-th layer has a constant thickness $\tau^{\langle\ell\rangle}$ and occupies the volume $V^{\langle\ell\rangle}$ with boundary $\partial V^{\langle\ell\rangle}$. The volume V of the shell is then the union of the layers' volumes $V = \cup_{\ell=1}^{N_\ell} V^{\langle\ell\rangle}$ and its boundary is denoted by ∂V. It follows that the shell thickness τ is given by $\tau \equiv \sum_{\ell=1}^{N_\ell} \tau^{\langle\ell\rangle}$.

In the remainder of the paper, the following conventions are adopted: a quantity referring to the ℓ-th layer is labelled with a superscript $\langle\ell\rangle$, Greek letter indices take values in the set $\{1, 2\}$, Latin letter indices take values in the set $\{1, 2, 3\}$, and repeated subscripts imply summation unless explicitly stated otherwise.

2.1. Geometry description

The geometry of the shell is defined starting from the equation of a generic point $\boldsymbol{x}_0 \in \mathbb{R}^3$ of its mid-surface

$$\boldsymbol{x}_0 = \boldsymbol{x}_0(\xi_1, \xi_2), \quad \text{for } \{\xi_1, \xi_2\} \in \Omega_\xi, \tag{1}$$

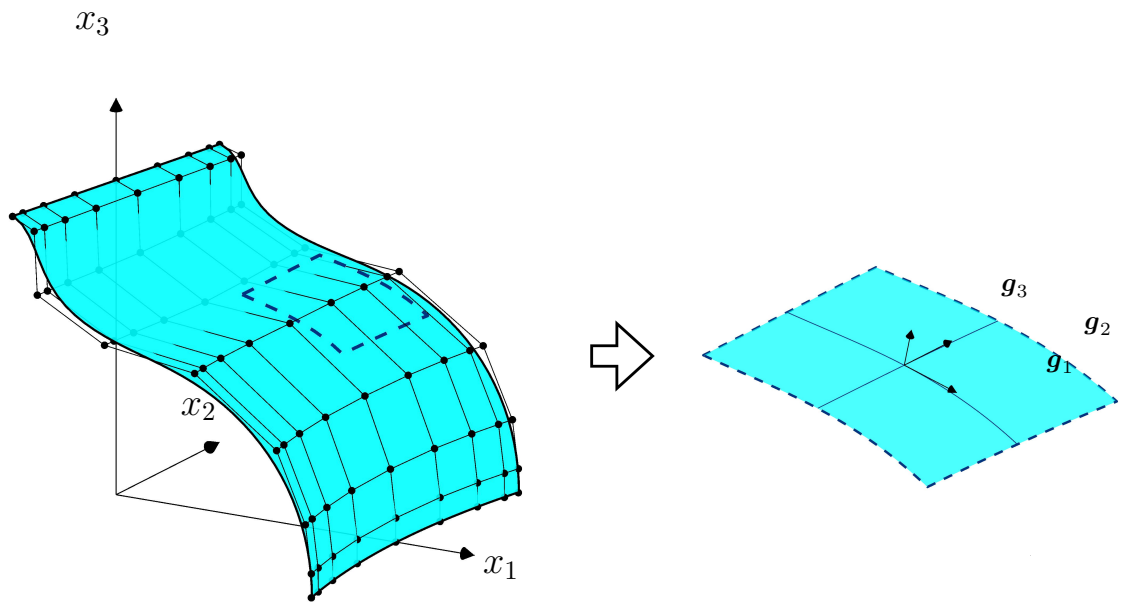

Figure 1: NURBS surface with its grid of control points and detail of the covariant basis at a generic surface location.

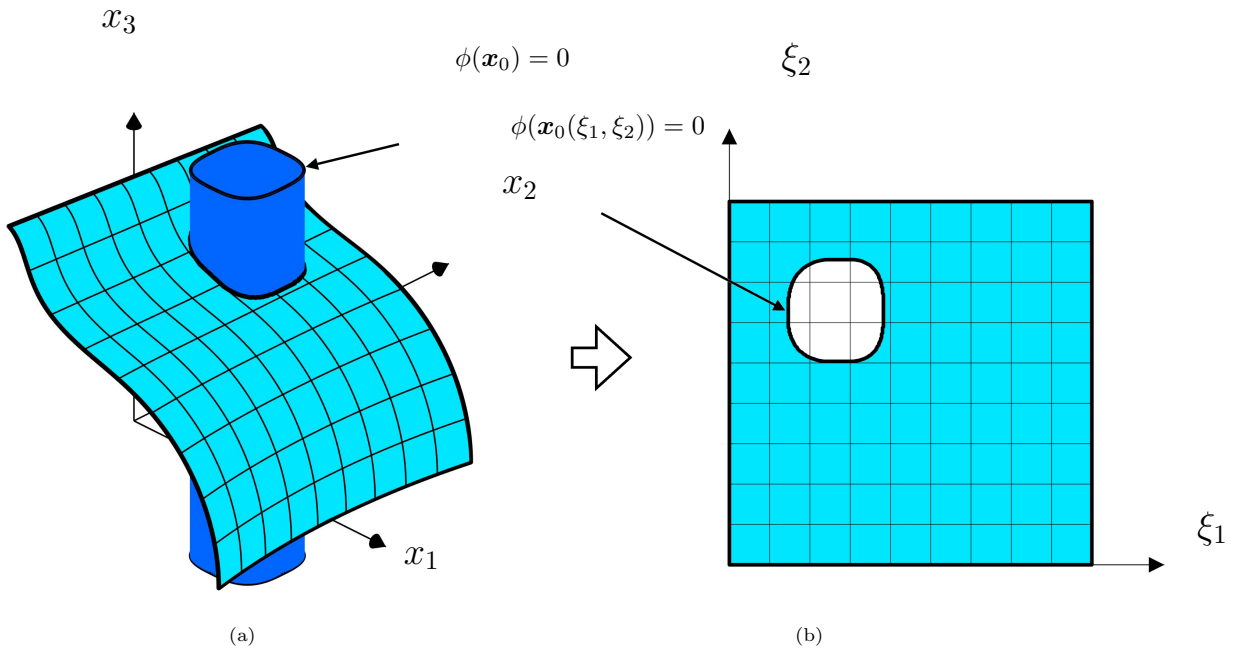

Figure 2: (a) Intersection between the zero-contour of the level set function and the shell mid-surface in $\mathbb{R}^3$. (b) Shell reference domain Ω_ξ implicitly defined by the level set function of figure (a).

where ξ_1 and ξ_2 are the two curvilinear variables spanning the shell's *reference domain* $\Omega_\xi \subset \mathbb{R}^2$. Using Eq.(1), the following vectors are introduced

$$\boldsymbol{a}_1 \equiv \frac{\partial \boldsymbol{x}_0}{\partial \xi_1}, \quad \boldsymbol{a}_2 \equiv \frac{\partial \boldsymbol{x}_0}{\partial \xi_2}, \quad \boldsymbol{a}_3 \equiv \boldsymbol{a}_1 \times \boldsymbol{a}_2, \quad \text{and} \quad \boldsymbol{n}_0 = \frac{\boldsymbol{a}_3}{||\boldsymbol{a}_3||}, \tag{2}$$

where $\boldsymbol{a}_1$ and $\boldsymbol{a}_2$ are tangent to the shell mid-surface and $\boldsymbol{n}_0$ is the orthogonal unit vector to the mid-surface. Then, the location of a generic point $\boldsymbol{x} \in \mathbb{R}^3$ of the shell's volume is given by

$$\boldsymbol{x}(\xi_1, \xi_2, \xi_3) \equiv \boldsymbol{x}_0(\xi_1, \xi_2) + \xi_3 \boldsymbol{n}_0(\xi_1, \xi_2), \quad \text{for } \{\xi_1, \xi_2, \xi_3\} \in \Omega_\xi \times I_{\xi_3}, \tag{3}$$

where $I_{\xi_3} \equiv [-\tau/2, \tau/2]$ is the interval spanned by the curvilinear variable ξ_3. With reference to Eq.(3), it is worth noting that the volume $V^{\langle \ell \rangle}$ of the generic ℓ-th layer is identified by $\boldsymbol{x} = \boldsymbol{x}(\xi_1, \xi_2, \xi_{3b}^{\langle \ell \rangle} \leq \xi_3 \leq \xi_{3t}^{\langle \ell \rangle})$ where $\xi_{3b}^{\langle \ell \rangle}$ and $\xi_{3t}^{\langle \ell \rangle}$ are the thickness coordinates of the ℓ-th layer's bottom and top surfaces, respectively.

Starting from the mapping given in Eq.(3), one defines the local *covariant basis*, whose i-th vector is defined as $\boldsymbol{g}_i \equiv \partial \boldsymbol{x} / \partial \xi_i$, and the local *contravariant basis*, whose i-th vector is defined $\boldsymbol{g}^i \cdot \boldsymbol{g}_j = \delta^i_j$ and δ^i_j is the Kronecker delta function. Additionally, the covariant components and the contravariant components of the metric tensor are defined as $g_{ij} \equiv \boldsymbol{g}_i \cdot \boldsymbol{g}_j$ and $g^{ij} \equiv \boldsymbol{g}^i \cdot \boldsymbol{g}^j$, respectively, while g denotes the determinant of g_{ij} [32]. Finally, the vectors of the contravariant basis can be collected in the columns of the matrix $\boldsymbol{R}$ such that the covariant components v_{ξ_i} and the Cartesian components v_i of a generic vector are related by

$$\boldsymbol{v} = \boldsymbol{R} \boldsymbol{v}_\xi, \tag{4}$$

where $\boldsymbol{v}_\xi \equiv \{v_{\xi_1}, v_{\xi_2}, v_{\xi_3}\}^\intercal$ and $\boldsymbol{v} \equiv \{v_1, v_2, v_3\}^\intercal$.

2.1.1. NURBS-based surface description

In the proposed method, Eq.(1) can be specified either in terms of a user-defined analytical function or in terms of a NURBS-based parametrizations. Both approaches are considered here since the former is suitable to generate simple geometries whereas the latter facilitates the coupling of the proposed method with modern CAD software libraries. However, while employing user-defined analytical functions does not require further details, it is worth recalling a few definitions for generally-curved surfaces represented via NURBS functions, which will be used in the numerical tests presented in Sec.(5). In this section, repeated subscripts do not imply summation.

The equation $\boldsymbol{x}_0 = \boldsymbol{x}_0(\xi_1, \xi_2)$ of a point $\boldsymbol{x}_0$ belonging to a NURBS surface in the 3D space is defined starting from a grid of $(n+1) \times (m+1)$ control points $\boldsymbol{P}_{ij}$ and a set of rational surface basis functions $S_{ij}(\xi_1, \xi_2)$ as follows

$$\boldsymbol{x}_0(\xi_1, \xi_2) \equiv \sum_{i=1}^{n+1} \sum_{j=1}^{m+1} \boldsymbol{P}_{ij} S_{ij}(\xi_1, \xi_2). \tag{5}$$

The rational basis functions $S_{ij}(\xi_1, \xi_2)$ are defined in terms of the one-dimensional B-spline basis functions as

$$S_{ij}(\xi_1, \xi_2) = \frac{h_{ij} N_{i,k}(\xi_1) M_{j,l}(\xi_2)}{\sum_{i=1}^{n+1} \sum_{j=1}^{m+1} h_{ij} N_{i,k}(\xi_1) M_{j,l}(\xi_2)}, \tag{6}$$

where h_{ij} is the weight of the point $\boldsymbol{P}_{ij}$, $N_{i,k}(\xi_1)$ is the i-th B-spline basis function in the direction ξ_1 with an order k and $M_{j,l}(\xi_2)$ is the j-th B-spline basis function in the direction ξ_2 with an order l. The B-spline basis functions are defined piece-wise in a recursive way accordingly to the Cox de Boor formula as

$$N_{i,1}(\xi) = \begin{cases} 1 & \text{for } \xi^i \leq \xi \leq \xi^{i+1} \\ 0 & \text{otherwise} \end{cases}, \tag{7a}$$

$$N_{i,k}(\xi) = \frac{(\xi - \xi^i) N_{i,k-1}(\xi)}{\xi^{i+k-1} - \xi^i} + \frac{(\xi^{i+k} - \xi) N_{i+1,k-1}(\xi)}{\xi^{i+k} - \xi^{i+1}}, \tag{7b}$$

where the ξ^i is a generic element of the so-called *knot vector* $\left\{\xi^1, \xi^2, \ldots, \xi^i, \ldots, \xi^{n+k+1}\right\}$, which is a sequence of non-decreasing value of the curvilinear variable and determines the intervals for the definition of the the basis functions. If the first and last values are repeated k times, the curve is interpolatory at the first and the last control points resulting in a B-spline with a so-called open knot vector. Figure (1) shows an example of a NURBS surface with the corresponding grid of control points (the black dots in the figure); the figure also shows the detail of the covariant basis at a generic location within the surface. The reader interested in a comprehensive description of the NURBS theory is referred to the books by Rogers [33] and by Piegl and Tiller [34].

2.1.2. Implicitly-defined cut-outs

Several approaches could be employed to resolve the presence of cut-outs in multilayered shells. For example, one could partition the shell reference domain Ω_ξ into multiple patches having different geometry descriptions, and then suitably combine them together. Here, to retain the relatively simple description of the shell mid-surface as given in Eq.(1), the cut-outs are implicitly-defined via a level set function of the curvilinear variables ξ_1 and ξ_2.

Consider a reference rectangle $\Pi_\xi \equiv [\xi_1^L, \xi_1^U] \times [\xi_2^L, \xi_2^U]$ spanned by the curvilinear variables ξ_1 and ξ_2, where ξ_α^L and ξ_α^U denotes the limits of the rectangle for the curvilinear variable ξ_α, and its boundary $\partial\Pi_\xi$. To exemplify, for a shell surface described by NURBS functions, Π_ξ is typically given by $[0,1] \times [0,1]$. Then, the reference domain Ω_ξ of a shell with cut-outs is defined as

$$\Omega_\xi \equiv \left\{ \{\xi_1, \xi_2\} \in \Pi_\xi \mid \phi(\xi_1, \xi_2) < 0 \right\}, \tag{8}$$

while its boundary $\partial\Omega_\xi$ is defined as

$$\partial\Omega_\xi \equiv \left\{ \{\xi_1, \xi_2\} \in \partial\Pi_\xi \mid \phi(\xi_1, \xi_2) < 0 \right\} \cup \Gamma_\xi, \tag{9}$$

where $\Gamma_\xi \equiv \{\{\xi_1, \xi_2\} \in \Pi_\xi |\ \phi(\xi_1, \xi_2) = 0\}$ denotes the boundary of the cut-out. It is clear that, for a shell *without* cut-outs, Ω_ξ and $\partial\Omega_\xi$ coincide with Π_ξ and $\partial\Pi_\xi$, respectively. Moreover, it is worth noting that the level set function can also be defined in the 3D space as $\phi = \phi(\boldsymbol{x}_0)$ and then expressed in terms of the curvilinear coordinates using Eq.(1), i.e. $\phi = \phi(\boldsymbol{x}_0(\xi_1, \xi_2)) = \phi(\xi_1, \xi_2)$. Figure (2a) shows an example of a case where a cut-out is defined by intersecting a generally-curved surface with a level set function $\phi = \phi(\boldsymbol{x}_0)$.

The corresponding implicitly-defined reference domain Ω_ξ is displayed in Fig.(2b). The discretization of a generic shell reference domain that is implicitly-defined using the approach described above is examined in Sec.(4).

2.2. Strain-displacement relations

Let $\boldsymbol{u} \equiv \{u_1, u_2, u_3\}^\intercal$ be the vector collecting the Cartesian components of the displacement field and $\boldsymbol{\gamma} \equiv \{\gamma_{11}, \gamma_{22}, \gamma_{33}, \gamma_{23}, \gamma_{13}, \gamma_{12}\}^\intercal$ be the vector collecting the Cartesian components of the strain field in Voigt notation. Then, within the small displacement assumption, the relationship between the displacement and the strain components is written in matrix form as follows

$$\boldsymbol{\gamma} = \boldsymbol{I}_i \frac{\partial \boldsymbol{u}}{\partial x_i}, \tag{10}$$

where the 6×3 matrices $\boldsymbol{I}_i$ are defined as

$$\boldsymbol{I}_1 \equiv \begin{bmatrix} 1 & 0 & 0 \\ 0 & 0 & 0 \\ 0 & 0 & 0 \\ 0 & 0 & 0 \\ 0 & 0 & 1 \\ 0 & 1 & 0 \end{bmatrix}, \quad \boldsymbol{I}_2 \equiv \begin{bmatrix} 0 & 0 & 0 \\ 0 & 1 & 0 \\ 0 & 0 & 0 \\ 0 & 0 & 1 \\ 0 & 0 & 0 \\ 1 & 0 & 0 \end{bmatrix} \quad \text{and} \quad \boldsymbol{I}_3 \equiv \begin{bmatrix} 0 & 0 & 0 \\ 0 & 0 & 0 \\ 0 & 0 & 1 \\ 0 & 1 & 0 \\ 1 & 0 & 0 \\ 0 & 0 & 0 \end{bmatrix}. \tag{11}$$

Upon using Eq.(4) in Eq.(10), the strain field can be expressed in terms of the covariant components $\boldsymbol{u}_\xi\{u_{\xi_1}, u_{\xi_2}, u_{\xi_3}\}^\intercal$ of the displacement fields as

$$\boldsymbol{\gamma} = \boldsymbol{I}_i \frac{\partial (\boldsymbol{R}\boldsymbol{u}_\xi)}{\partial x_i} = \boldsymbol{I}_i \left(\frac{\partial \boldsymbol{R}}{\partial \xi_j} \boldsymbol{u}_\xi + \boldsymbol{R} \frac{\partial \boldsymbol{u}_\xi}{\partial \xi_j} \right) \frac{\partial \xi_j}{\partial x_i}, \tag{12}$$

where the second equality is obtained via a mere application of the chain rule for differentiation. It is worth noting that the matrix $\boldsymbol{R}$ and its derivatives $\partial \boldsymbol{R}/\partial \xi_j$ are determined once an explicit expression for the shell mid-surface equation given in Eq.(1) is chosen. In fact, as briefly discussed in Appendix Appendix A, they are obtained in terms of the derivatives of the map given in Eq.(1) with respect to the curvilinear coordinates ξ_1 and ξ_2 up to third order.

2.3. Constitutive behavior

The constitutive behavior of a generic ℓ-th layer of the multilayered shells is assumed to be orthotropic in a reference system identified by the unit vectors $\boldsymbol{m}_1^{\langle \ell \rangle}$, $\boldsymbol{m}_2^{\langle \ell \rangle}$ and $\boldsymbol{m}_3^{\langle \ell \rangle}$. At the generic point $\boldsymbol{x} \in V^{\langle \ell \rangle}$, such a reference system is determined as follows: $\boldsymbol{m}_3^{\langle \ell \rangle}$ coincides with $\boldsymbol{n}_0$; $\boldsymbol{m}_1^{\langle \ell \rangle}$ is defined as

$$\boldsymbol{m}_1^{\langle \ell \rangle} \equiv \boldsymbol{R}_{\boldsymbol{a}_3}(\theta^{\langle \ell \rangle}) \frac{\boldsymbol{g}_1}{||\boldsymbol{g}_1||}, \tag{13}$$

where the matrix $\boldsymbol{R}_{\boldsymbol{a}_3}(\theta^{\langle \ell \rangle})$ performs a rotation around the axis $\boldsymbol{n}_0$ of the *lamination angle* $\theta^{\langle \ell \rangle}$ between the covariant basis vector $\boldsymbol{g}_1$ and fiber orientation of the ℓ-th layer $\boldsymbol{m}_1^{\langle \ell \rangle}$; and $\boldsymbol{m}_2^{\langle \ell \rangle} \equiv \boldsymbol{m}_3^{\langle \ell \rangle} \times \boldsymbol{m}_1^{\langle \ell \rangle}$. In this

orthotropic reference system, the relationship between the components of the stress field $\widetilde{\boldsymbol{\sigma}}^{\langle\ell\rangle}$, also expressed in Voigt notation, and the strain field $\widetilde{\boldsymbol{\gamma}}^{\langle\ell\rangle}$ is given by

$$\widetilde{\boldsymbol{\sigma}}^{\langle\ell\rangle} = \widetilde{\boldsymbol{c}}^{\langle\ell\rangle}\widetilde{\boldsymbol{\gamma}}^{\langle\ell\rangle}, \tag{14}$$

where $\widetilde{\boldsymbol{c}}^{\langle\ell\rangle}$ is a 6×6 matrix whose elements are expressed in terms of the engineering constants [1]. The relationship between the components of the stress field $\boldsymbol{\sigma}^{\langle\ell\rangle}$ and the strain field $\boldsymbol{\gamma}^{\langle\ell\rangle}$ in the global Cartesian reference system is finally given as

$$\boldsymbol{\sigma}^{\langle\ell\rangle} = \boldsymbol{c}^{\langle\ell\rangle}\boldsymbol{\gamma}^{\langle\ell\rangle}, \tag{15}$$

where the matrix $\boldsymbol{c}^{\langle\ell\rangle}$ is obtained from $\widetilde{\boldsymbol{c}}^{\langle\ell\rangle}$ by standard transformation procedures [35].

2.4. The Equivalent-Single-Layer theory for shells

In the context of displacement-based Equivalent-Single-Layer theories for multilayered plates and shells, see e.g. [36, 9] and the references cited therein, suitable assumptions are introduced for the behavior of the displacement field along the thickness of the multilayered structure. Here, it is assumed that the covariant components u_{ξ_i} of the displacement field may be written as

$$u_{\xi_i}^{\langle\ell\rangle}(\xi_1, \xi_2, \xi_3) = \sum_{k=0}^{N_i} U_{ik}(\xi_1, \xi_2) f_k(\xi_3), \quad \forall \ell = 1, \ldots, N_\ell. \tag{16}$$

where f_k are known arbitrary functions of the thickness coordinate ξ_3, U_{ik} represent the new variables called *generalized displacements* and N_i is the order of the expansion for the i-th displacement component. It is noted that, consistently with ESL theories, Eq.(16) provides a through-the-thickness expansion of the displacement components that is valid for all layers of the shell. This is why f_k and U_{ik} are not labelled with the subscript $\langle\ell\rangle$.

Following the notation introduced in [28, 29, 31], Eq.(16) is written in a more compact form as

$$\boldsymbol{u}_{\xi}^{\langle\ell\rangle} = \boldsymbol{F}(\xi_3)\boldsymbol{U}(\xi_1, \xi_2), \quad \forall \ell = 1, \ldots, N_\ell, \tag{17}$$

where $\boldsymbol{F}$ is a $3 \times N_U$ matrix that opportunely collects the functions f_k, and $\boldsymbol{U}$ is a $N_U \times 1$ vector containing the generalized displacements being $N_U \equiv (N_1 + N_2 + N_3 + 3)$.

Combining Eq.(17) and Eq.(12), the strain in Cartesian coordinates is obtained in terms of the generalized displacements as

$$\boldsymbol{\gamma}^{\langle\ell\rangle} = \boldsymbol{J}_0\boldsymbol{U} + \boldsymbol{J}_\alpha \frac{\partial \boldsymbol{U}}{\partial \xi_\alpha}, \quad \forall \ell = 1, \ldots, N_\ell, \tag{18}$$

where the following matrices have been introduced

$$\boldsymbol{J}_0 \equiv \boldsymbol{I}_i \left(\frac{\partial \xi_j}{\partial x_i} \frac{\partial \boldsymbol{R}}{\partial \xi_j}\boldsymbol{F} + \frac{\partial \xi_3}{\partial x_i}\boldsymbol{R}\frac{\mathrm{d}\boldsymbol{F}}{\mathrm{d}\xi_3} \right) \quad \text{and} \quad \boldsymbol{J}_\alpha \equiv \boldsymbol{I}_i \frac{\partial \xi_\alpha}{\partial x_i}\boldsymbol{R}\boldsymbol{F}. \tag{19}$$

Eventually, taking into account Eq.(15), the following expression is obtained for the stress in Cartesian coordinates

$$\boldsymbol{\sigma}^{\langle\ell\rangle} = \boldsymbol{c}^{\langle\ell\rangle} \left(\boldsymbol{J}_0\boldsymbol{U} + \boldsymbol{J}_\alpha \frac{\partial \boldsymbol{U}}{\partial \xi_\alpha} \right), \quad \ell = 1, \ldots, N_\ell, \tag{20}$$

where, unlike the expression of the displacement and the strain fields given in Eqs.(17) and (18), respectively, it is clear that the stress field is discontinuous between adjacent layers.

2.5. Governing equations

In the preceding section, the displacement field, the strain field and the stress field have been expressed as functions of the generalized displacements, which are collected in the vector $\boldsymbol{U}$ and represent the primary unknowns of the multilayered shell problem. Then, it is possible to show [31] that the static behavior of a multilayered shell modelled by ESL theories is governed by the following set of differential equations

$$-\frac{\partial}{\partial\xi_\alpha}\left(\boldsymbol{Q}_{\alpha\beta}\frac{\partial\boldsymbol{U}}{\partial\xi_\beta}+\boldsymbol{R}_{\alpha3}\boldsymbol{U}\right)+\boldsymbol{R}_{\alpha3}^{\intercal}\frac{\partial\boldsymbol{U}}{\partial\xi_\alpha}+\boldsymbol{S}_{33}\boldsymbol{U}=\overline{\boldsymbol{B}},\quad\text{in }\Omega_\xi, \tag{21}$$

and the following set of boundary conditions

$$\begin{cases}\nu_\alpha\left(\boldsymbol{Q}_{\alpha\beta}\frac{\partial\boldsymbol{U}}{\partial\xi_\beta}+\boldsymbol{R}_{\alpha3}\boldsymbol{U}\right)=\overline{\boldsymbol{T}}, & \text{on }\partial\Omega_{\xi N}\\ \boldsymbol{U}=\overline{\boldsymbol{U}}, & \text{on }\partial\Omega_{\xi D}\end{cases}, \tag{22}$$

where ν_α is the α-th component of the unit vector perpendicular to the boundary $\partial\Omega_\xi$ of the shell reference domain Ω_ξ, and $\partial\Omega_{\xi D}$ and $\partial\Omega_{\xi N}$ are the portions of the boundary where kinematic and mechanical boundary conditions are applied, respectively. Additionally, in Eqs.(21) and (22), the following generalized stiffness matrix, volume loads and boundary loads have been defined

$$\boldsymbol{Q}_{\alpha\beta}\equiv\sum_{\ell=1}^{N_\ell}\int_{\xi_{3b}^{\langle\ell\rangle}}^{\xi_{3t}^{\langle\ell\rangle}}\boldsymbol{J}_\alpha^{\intercal}\boldsymbol{c}^{\langle\ell\rangle}\boldsymbol{J}_\beta\sqrt{g}\;\mathrm{d}\xi_3, \tag{23a}$$

$$\boldsymbol{R}_{\alpha3}\equiv\sum_{\ell=1}^{N_\ell}\int_{\xi_{3b}^{\langle\ell\rangle}}^{\xi_{3t}^{\langle\ell\rangle}}\boldsymbol{J}_\alpha^{\intercal}\boldsymbol{c}^{\langle\ell\rangle}\boldsymbol{J}_0\sqrt{g}\;\mathrm{d}\xi_3, \tag{23b}$$

$$\boldsymbol{S}_{33}\equiv\sum_{\ell=1}^{N_\ell}\int_{\xi_{3b}^{\langle\ell\rangle}}^{\xi_{3t}^{\langle\ell\rangle}}\boldsymbol{J}_0^{\intercal}\boldsymbol{c}^{\langle\ell\rangle}\boldsymbol{J}_0\sqrt{g}\;\mathrm{d}\xi_3. \tag{23c}$$

$$\overline{\boldsymbol{B}}\equiv\left(\boldsymbol{F}^{\intercal}\boldsymbol{R}^{\intercal}\overline{\boldsymbol{t}}\sqrt{g}\sqrt{n_ig^{ij}n_j}\right)_{\xi_3=\pm\tau/2}+\sum_{\ell=1}^{N_\ell}\int_{\xi_{3b}^{\langle\ell\rangle}}^{\xi_{3t}^{\langle\ell\rangle}}\boldsymbol{F}^{\intercal}\boldsymbol{R}^{\intercal}\overline{\boldsymbol{b}}\sqrt{g}\;\mathrm{d}\xi_3, \tag{24a}$$

$$\overline{\boldsymbol{T}}\equiv\sum_{\ell=1}^{N_\ell}\int_{\xi_{3b}^{\langle\ell\rangle}}^{\xi_{3t}^{\langle\ell\rangle}}\boldsymbol{F}^{\intercal}\boldsymbol{R}^{\intercal}\overline{\boldsymbol{t}}^{\langle\ell\rangle}\sqrt{g}\sqrt{n_ig^{ij}n_j}\;\mathrm{d}\xi_3, \tag{24b}$$

where n_i is the i-th Cartesian component of the outer unit normal at a boundary of the shell volume V. The interested reader is referred to Ref.[31] for a detailed derivation of Eqs.(21) and (22) and the related generalized quantities.

3. Interior Penalty discontinuous Galerkin formulation

The solution of the governing equations given in Sec.(2.5) is based on the Interior Penalty discontinuous Galerkin formulation recently proposed for multilayered plates and shells [28, 29, 31] and recalled in this section for the sake of completeness.

The domain Ω_ξ is divided into N_e non-overlapping elements, which constitute the mesh and where the generic e-th element has domain $\Omega_\xi^{(e)}$ and boundary $\partial\Omega_\xi^{(e)}$. In the following, quantities associated to the e-th

element are denoted by the subscript (e). Over the mesh, the space $\mathcal{V}_{hp}$ of discontinuous polynomial basis functions of maximum degree p is introduced as

$$\mathcal{V}_{hp} \equiv \left\{ v : \Omega_\xi \to \mathbb{R} \mid v|_{\Omega_\xi^{(e)}} \in \mathcal{P}_p^{(e)} \ \forall e = 1, ..., N_e \right\}, \tag{25}$$

where $\mathcal{P}_p^{(e)}$ is the space of polynomials with maximum degree p. Similarly, the space $\mathcal{V}_{hp}^{N_U}$ of discontinuous polynomial vector field is defined as $\mathcal{V}_{hp}^{N_U} \equiv (\mathcal{V}_{hp})^{N_U}$. Then, following Refs.[28, 29, 31], the Interior Penalty dG formulation for Eqs.(21) and (22) reads

$$B(\boldsymbol{V}, \boldsymbol{U}_h) = F(\boldsymbol{V}, \overline{\boldsymbol{B}}, \overline{\boldsymbol{T}}, \overline{\boldsymbol{U}}), \quad \forall \boldsymbol{V} \in \mathcal{V}_{hp}^{N_U}, \tag{26}$$

where $\boldsymbol{U}_h$ denotes the approximate dG solution of Eqs.(21) and (22), and the bilinear form $B(\boldsymbol{V}, \boldsymbol{U}_h)$ and the linear form $F(\boldsymbol{V}, \overline{\boldsymbol{B}}, \overline{\boldsymbol{T}}, \overline{\boldsymbol{U}})$ have the following expressions

$$\begin{aligned} B(\boldsymbol{V}, \boldsymbol{U}_h) \equiv & \int_{\Omega_h} \frac{\partial \boldsymbol{V}^\intercal}{\partial \xi_\alpha} \left(\boldsymbol{Q}_{\alpha\beta} \frac{\partial \boldsymbol{U}_h}{\partial \xi_\beta} + \boldsymbol{R}_{\alpha 3} \boldsymbol{U}_h \right) + \boldsymbol{V}^\intercal \left(\boldsymbol{R}_{\alpha 3}^\intercal \frac{\partial \boldsymbol{U}_h}{\partial \xi_\alpha} + \boldsymbol{S}_{33} \boldsymbol{U}_h \right) + \\ & - \int_{\partial\Omega_{hI}} [\![\boldsymbol{V}]\!]_\alpha^\intercal \left\{ \boldsymbol{Q}_{\alpha\beta} \frac{\partial \boldsymbol{U}_h}{\partial \xi_\beta} + \boldsymbol{R}_{\alpha 3} \boldsymbol{U}_h \right\} + \left\{ \frac{\partial \boldsymbol{V}^\intercal}{\partial \xi_\alpha} \boldsymbol{Q}_{\alpha\beta} + \boldsymbol{V}^\intercal \boldsymbol{R}_{\beta 3}^\intercal \right\} [\![\boldsymbol{U}_h]\!]_\beta + \\ & - \int_{\partial\Omega_{hD}} \nu_\alpha \boldsymbol{V}^\intercal \left(\boldsymbol{Q}_{\alpha\beta} \frac{\partial \boldsymbol{U}_h}{\partial \xi_\beta} + \boldsymbol{R}_{\alpha 3} \boldsymbol{U}_h \right) + \left(\frac{\partial \boldsymbol{V}^\intercal}{\partial \xi_\alpha} \boldsymbol{Q}_{\alpha\beta} + \boldsymbol{V}^\intercal \boldsymbol{R}_{\beta 3}^\intercal \right) \boldsymbol{U}_h \nu_\beta + \\ & + \int_{\partial\Omega_{hI}} \mu [\![\boldsymbol{V}]\!]_\alpha^\intercal [\![\boldsymbol{U}_h]\!]_\alpha + \int_{\partial\Omega_{hD}} \mu \boldsymbol{V}^\intercal \boldsymbol{U}_h \end{aligned} \tag{27}$$

and

$$F(\boldsymbol{V}, \overline{\boldsymbol{B}}, \overline{\boldsymbol{T}}, \overline{\boldsymbol{U}}) \equiv \int_{\Omega_h} \boldsymbol{V}^\intercal \overline{\boldsymbol{B}} + \int_{\partial\Omega_{hN}} \boldsymbol{V}^\intercal \overline{\boldsymbol{T}} - \int_{\partial\Omega_{hD}} \left(\frac{\partial \boldsymbol{V}^\intercal}{\partial \xi_\alpha} \boldsymbol{Q}_{\alpha\beta} + \boldsymbol{V}^\intercal \boldsymbol{R}_{\beta 3}^\intercal \right) \overline{\boldsymbol{U}} \nu_\beta + \int_{\partial\Omega_{hD}} \mu \boldsymbol{V}^\intercal \overline{\boldsymbol{U}}. \tag{28}$$

The integrals appearing in Eqs.(27) and (28) are usually referred to as *broken integrals* and are defined as

$$\int_{\Omega_h} \bullet \equiv \sum_{e=1}^{N_e} \int_{\Omega_\xi^{(e)}} \bullet^{(e)} \, \mathrm{d}\Omega_\xi \tag{29a}$$

and

$$\int_{\partial\Omega_{hI}} \bullet \equiv \sum_{i=1}^{N_i} \int_{\partial\Omega_{\xi I}^{(i)}} \bullet^{(i)} \, \mathrm{d}\partial\Omega_\xi, \quad \int_{\partial\Omega_{hD}} \bullet \equiv \sum_{e=1}^{N_e} \int_{\partial\Omega_{\xi D}^{(e)}} \bullet^{(e)} \, \mathrm{d}\partial\Omega_\xi, \quad \int_{\partial\Omega_{hN}} \bullet \equiv \sum_{e=1}^{N_e} \int_{\partial\Omega_{\xi N}^{(e)}} \bullet^{(e)} \, \mathrm{d}\partial\Omega_\xi, \tag{29b}$$

where $\partial\Omega_{\xi I}^{(i)}$ denotes the generic i-th interface between two adjacent elements, $\partial\Omega_{\xi D}^{(e)}$ is the portion of $\partial\Omega_\xi^{(e)}$ where kinematic boundary conditions are enforced and $\partial\Omega_{\xi N}^{(e)}$ is the portion of $\partial\Omega_\xi^{(e)}$ where mechanical boundary conditions are enforced. Additionally, in Eqs.(27) and (28), μ is the *penalty parameter*, while $\{\bullet\}$ and $[\![\bullet]\!]_\alpha$ are the *average* and *jump* operators, respectively, defined as

$$\{\bullet\}^{(i)} \equiv \frac{1}{2} \left(\bullet^{(e)} + \bullet^{(e')} \right) \quad \text{and} \quad [\![\bullet]\!]_\alpha^{(i)} \equiv \nu_\alpha^{(e)} \bullet^{(e)} + \nu_\alpha^{(e')} \bullet^{(e')}, \tag{30}$$

being e and e' the indices of two adjacent elements sharing the interface boundary i.

The interested reader is referred to Refs.[28, 29, 31] for a detailed derivation of the Interior Penalty dG formulation employed in this work.

4. Implicitly-defined mesh

The discontinuous Galerkin formulation described in Sec.(3) is not limited to a specific choice of the type of mesh elements and could be used in combination with different discretization strategies (including, e.g., triangular or polygonal elements) provided that the corresponding quadrature rules to evaluate the integrals appearing in Eqs.(27) and (28) may be available.

In this work, with reference to the implicit representation of the shell reference domain Ω_ξ as discussed in Sec.(2.1.2), the discretization of Ω_ξ is obtained by intersecting a structured background grid and the level set function $\phi = \phi(\xi_1, \xi_2)$. Let $C_\xi^{(e)}$ denote a generic cell of the background grid generated for the reference rectangle Π_ξ and $\partial C_\xi^{(e)}$ denote its boundary. Then, the domain $\Omega_\xi^{(e)}$ and the boundary $\partial\Omega_\xi^{(e)}$ of the corresponding *implicitly-defined* mesh element are defined as

$$\Omega_\xi^{(e)} = C_\xi^{(e)} \cap \Omega_\xi \quad \text{and} \quad \partial\Omega_\xi^{(e)} = (\partial C_\xi^{(e)} \cap \Omega_\xi) \cup (C_\xi^{(e)} \cap \Gamma_\xi). \tag{31}$$

It follows that the implicitly-defined elements are classified into the following groups: the group of *entire* elements, which fall completely inside the shell reference domain Ω_ξ; the group of *empty* elements, which fall completely outside Ω_ξ and the group of *partial* elements, which are cut by Γ_ξ. Because of the arbitrariness of the level set function, *partial* elements may include elements with a very small volume fraction, which are then referred to as *small* elements. Small elements can cause an ill-conditioning of the final linear system and, therefore, they are merged with nearby entire elements or partial elements with a sufficiently large volume fraction. Entire and partial elements used in the merging strategy are then referred to as *extended* elements. Figure (3a) shows the element classification when a 9×9 background grid is employed to initially subdivide the reference rectangle Π_ξ, whereas Fig.(3b) shows the corresponding implicitly-defined mesh after the small elements have been merged with their neighbors. As a final remark, it is worth stressing that the domain and the boundary integrals appearing in Eqs.(27) and (28) require suitable quadrature rules. For entire elements, which comprise the majority of the mesh elements, these integrals are evaluated using high-order tensor-product Gauss-Legendre quadrature rules. On the other hand, the domain and the boundary integrals over partial elements and element boundaries are evaluated using the high-order quadrature rules obtained using the algorithm developed by Saye [37].

5. Numerical results

In this section, the capabilities of the presented formulation are assessed by testing the static response of a cylindrical multilayered shell and a generally-curved NURBS-based multilayered shell with a cut-out. High-order Legendre polynomials are used for both as thickness function of the considered ESL theories and as basis functions of the Interior Penalty dG scheme. To identify the adopted shell theory, the following notation is adopted: $\text{ED}_{N_1N_2N_3}$ denotes the ESL theory with an order of expansion N_1, N_2 and N_3 for the covariant components u_{ξ_1}, u_{ξ_2} and u_{ξ_3}, respectively, of the displacement field. On the other hand, the dG scheme is identified by order p of the polynomial basis functions. The FSDT is also considered by choosing

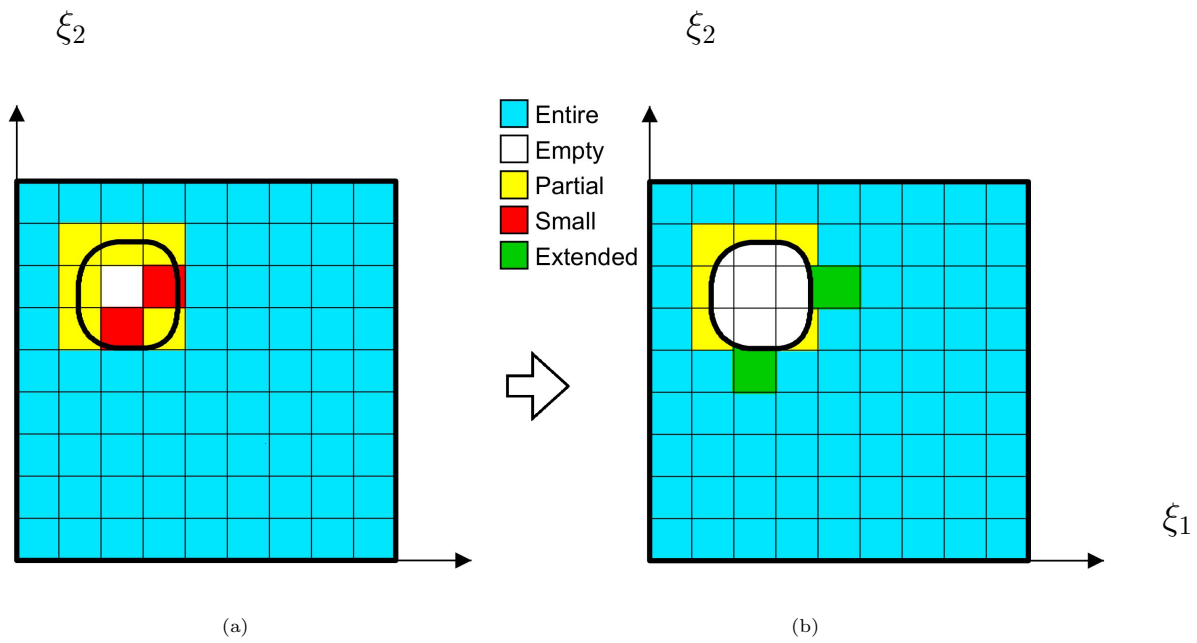

Figure 3: (a) Element classification according to their volume fraction. (b) Resulting mesh after the cell-merging strategy.

the ED_{110} and introducing the plane stress hypothesis. The properties of the considered shell sections and materials are reported in Tab.(2) and Tab.(3), respectively. The obtained results are eventually compared with those obtained with the FEM library Abaqus [38].

5.1. Fuselage panel with window

The first geometry investigated is a cylindrical shell with a cut-out as shown in Fig.(4). The dimensions and the level set are chosen in order to resemble a fuselage panel with a window. The reference surface is

Table 1: Quantities entering the parametric equation of the considered shell reference surfaces.

Fuselage panel		**NURBS-based shell**	
R_f	3 m	H_n	50 cm
θ_f	$\pi/12$	D_n	5 cm
L_f	60 cm	L_n	60 cm
a_f	15 cm	a_n	8.5 cm
b_f	22.5 cm	d_n	3
d_f	3	x_{1n}	15 cm
		x_{2n}	12 cm

Table 2: Properties of the considered shell sections.

Shell ID	**Material**	**Layup**	**Layer(s) thickness**
F_1 (Single-layer)	M_1	[0]	10 cm
F_2 (Single-layer)	M_2	[0]	10 cm
F_3 (Multilayered)	M_2	$[0/90]_s$	1 mm
F_4 (Multilayered)	M_2	$[+45/-45]_2$	1 mm
N_1 (Single-layer)	M_1	[0]	1 mm
N_2 (Multilayered)	M_2	$[0/90]_s$	1 mm

Table 3: Properties of the considered materials.

Material ID	**Property**	**Component**	**Value**
M_1 (Isotropic)	Young's modulus	E/E_r	1
	Poisson's ratio	ν	0.25
M_2 (Orthotropic)	Young's moduli	E_1/E_r	25
		E_2/E_r, E_3/E_r	1
	Poisson's ratios	ν_{23}, ν_{13}, ν_{12}	0.25
	Shear moduli	G_{23}/E_r	0.2
		G_{13}/E_r, G_{12}/E_r	0.5

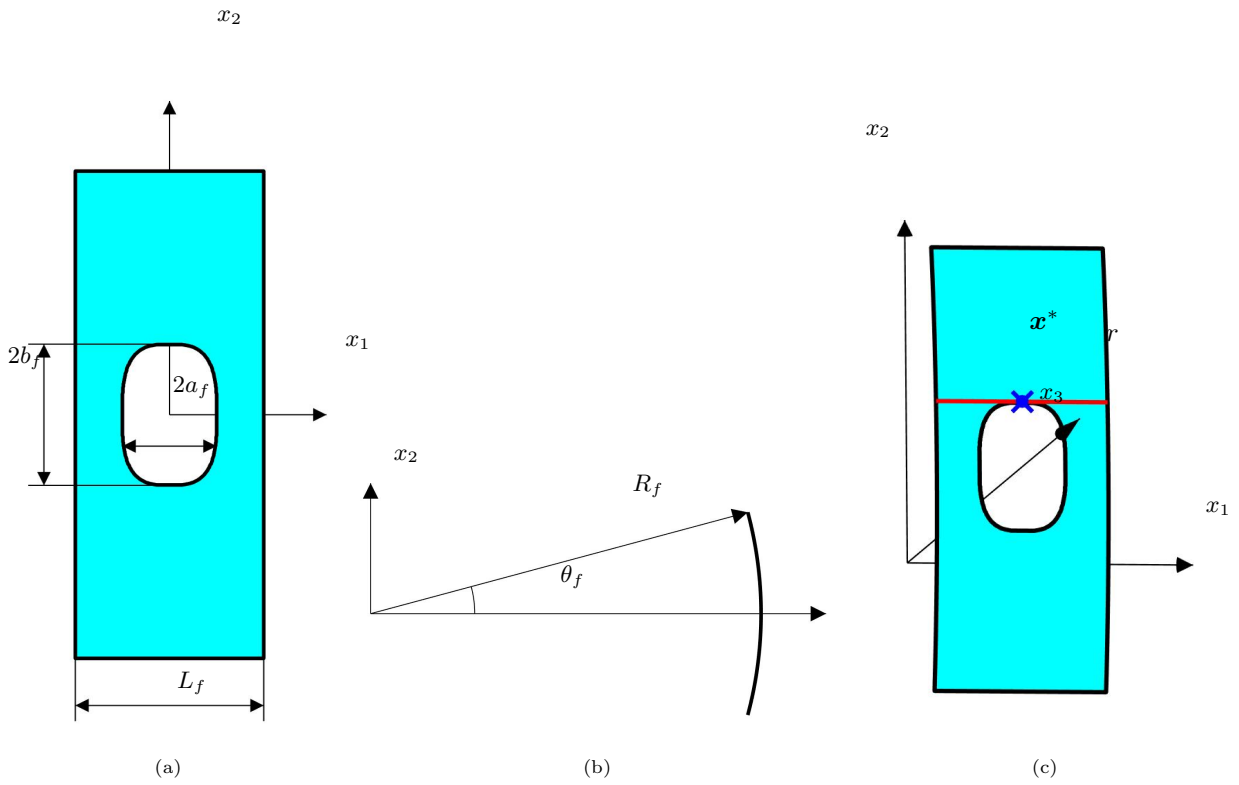

Figure 4: Geometry of the fuselage panel with a window in three different views.

mapped by the equation

$$\boldsymbol{x}_0 = \begin{bmatrix} \xi_1 \\ R_f \sin(\xi_2) \\ R_f \cos(\xi_2) \end{bmatrix}, \tag{32}$$

where $\xi_1 \in [-L_f/2, +L_f/2]$ and $\xi_2 \in [-\theta_f, +\theta_f]$ and R_f, L_f and θ_f are reported in Tab.(1). The level set function used to define the cut-out is chosen as

$$\phi(\boldsymbol{x}_0) = a_f^{d_f} - |x_{01}|^{d_f} - \left| \frac{x_{02}}{b_f/a_f} \right|^{d_f}, \tag{33}$$

where a_f, b_f and d_f are also reported in Tab.(1). The shell has clamped external boundaries, traction-free boundary conditions along the cut-out, and is subjected to a uniform pressure on the bottom surface identified by $\boldsymbol{x} = \boldsymbol{x}(\xi_1, \xi_2, -\tau_f/2)$ as

$$\bar{\boldsymbol{t}} = -q_f \boldsymbol{g}^3. \tag{34}$$

The four shell sections labelled as F_1 to F_4 in Tab.(2) are investigated, and the following non-dimensional magnitude of the displacement is introduced

$$|\overline{u}| \equiv |u| \cdot \left(\frac{\tau_f^3 E_r}{(L_f/2)^4 q_f} \right). \tag{35}$$

Consider the point $\boldsymbol{x}^*$ in Fig.(4c) corresponding to $\xi_1 = \xi_3 = 0$ and $\xi_2 = \alpha = \arcsin(b_f/R_f)$. The value of $|\overline{u}|$ at $\boldsymbol{x}^*$ is computed using the FSDT and the ED_{444} theory and a dG scheme with polynomial order

$p = 4$, and is then compared with the value evaluated at the same location computed using Abaqus S4R shell elements and C3D20R brick elements. Figures (5a), (5b), (5c) and (5d) report the obtained results as functions of the overall number of degrees of freedom of the discrete system for the shell sections F_1, F_2, F_3 and F_4, respectively, and show how the proposed scheme is able to recover the FEM results. Moreover, by looking at Fig.(5a), which corresponds to the case of the isotropic shell, one observes no noticeable difference in the values of the displacement magnitude computed with the FSDT, the ED_{444} theory and the 3D FEM model; differently, considering Fig.(5b), which corresponds to the case of the orthotropic shell, it is clear how the high-order ED_{444} reproduces more adequately the 3D FEM solution with respect to the low-order FSDT.

The effect of the polynomial order p on the value of the non-dimensional displacement magnitude $|\overline{u}|$ evaluated at the same point $\boldsymbol{x}^* = \boldsymbol{x}(0, \alpha, 0)$ is shown in Fig.(6); Fig.(6a) is referred to the shell section F_2 modelled with the ED_{444} theory, while Fig.(6b) is referred to the shell section F_3 modelled with the FSDT. In both cases, as expected, using $p = 6$ allows obtaining the converged solution with the smallest number of degrees of freedom, whereas using $p = 2$ shows the slowest convergence rate.

Figure (7) shows the value of the non-dimensional displacement magnitude $|\overline{u}|$ as given in Eq.(35) along the curve identified by varying ξ_1 and by keeping constant $\xi_2 = \alpha$ and $\xi_3 = 0$; the curve is indicated as r in Fig.(4c). Figures (7a), (7b), (7c) and (7d) are referred to the shell sections F_1, F_2, F_3 and F_4, respectively. In all figures, the results referring to the present approach are obtained using the FSDT theory and a dG scheme with polynomial order $p = 4$, whereas the reference solution (the dashed line in the figure) is obtained using Abaqus S4R shell elements. Also in this case, the obtained results confirm the accuracy of the proposed method.

The effect of the mesh size on the value of $|\overline{u}|$ evaluated along the same curve using the FSDT theory and a dG scheme with polynomial order $p = 2$ is presented in Figs.(8a) and (8b) for the shell sections F_2 and F_3, respectively. Here, it is interesting to note that the multilayered shell displays a slower convergence rate as a function of the number of cells in the background grid with respect to the case of the homogeneous orthotropic shell.

As a concluding remark for the cylindrical shell test, the contour plots of the non-dimensional displacement magnitude as given in Eq.(35) and two selected stress measures are shown in Fig.(9), where they are superimposed on the deformed shape of the top surface of the shell. In particular, Fig.(9a) shows the contour plot of the non-dimensional displacement magnitude for the shell sections F_1, Fig.(9b) shows the contour plot of the non-dimensional displacement magnitude for the shell sections F_3, Fig.(9c) shows the contour plot of the non-dimensional Von Mises stress $\overline{\sigma}_m$ for the shell sections F_1, and Fig.(9d) shows the contour plot of the non-dimensional stress component $\overline{\sigma}_{11}$ for the shell sections F_3. To compute the stress measures introduced above, the stress components are non-dimensional accordingly to the equation

$$\overline{\sigma}_{ij} \equiv \sigma_{ij} \cdot \left(\frac{\tau_f^2}{(L_f/2)^2 q_f} \right), \tag{36}$$

where σ_{ij} is a generic component of $\boldsymbol{\sigma}$.

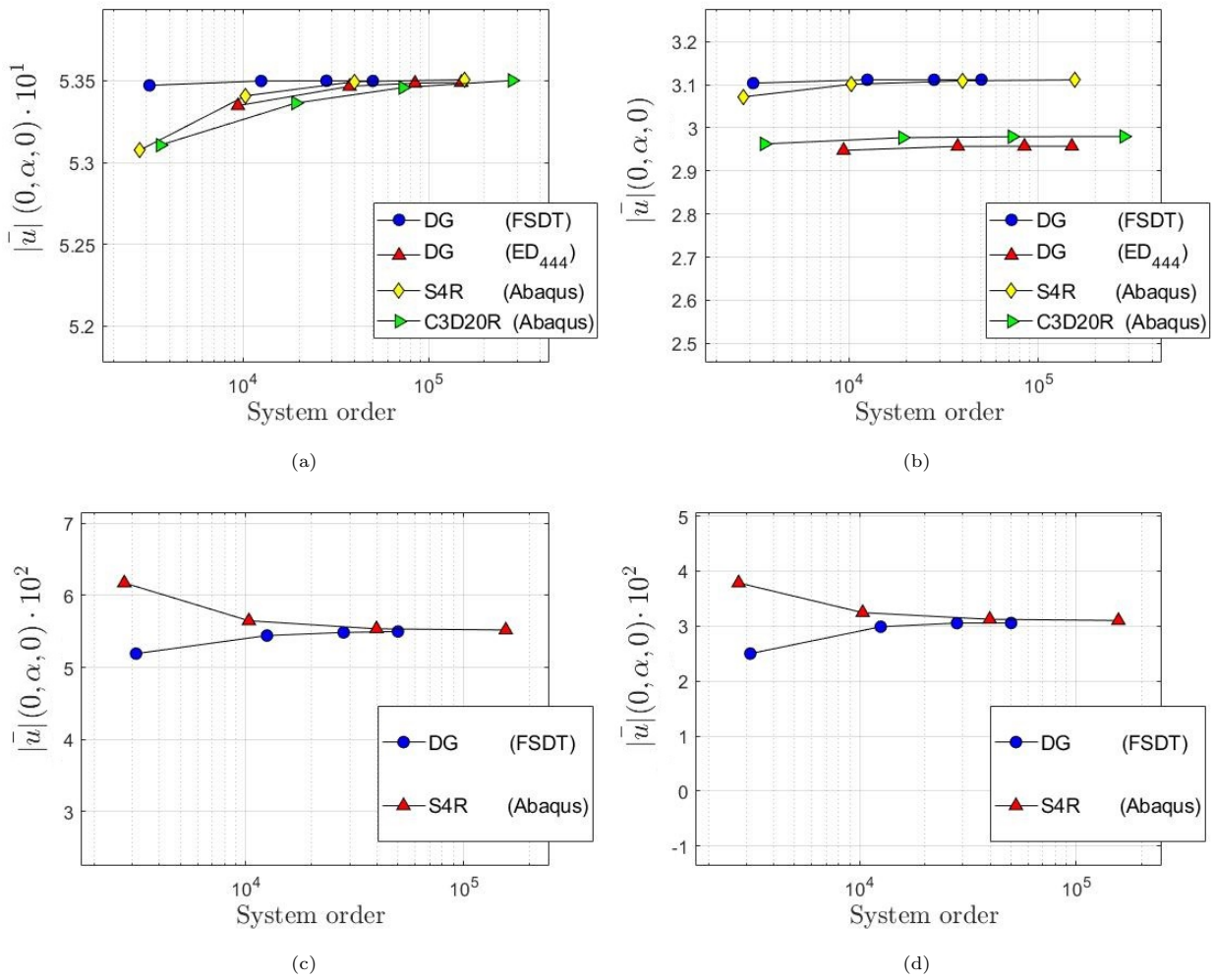

Figure 5: Comparison between the convergence of the FEM solution and the convergence of the solution obtained by the present formulation for the fuselage panel.

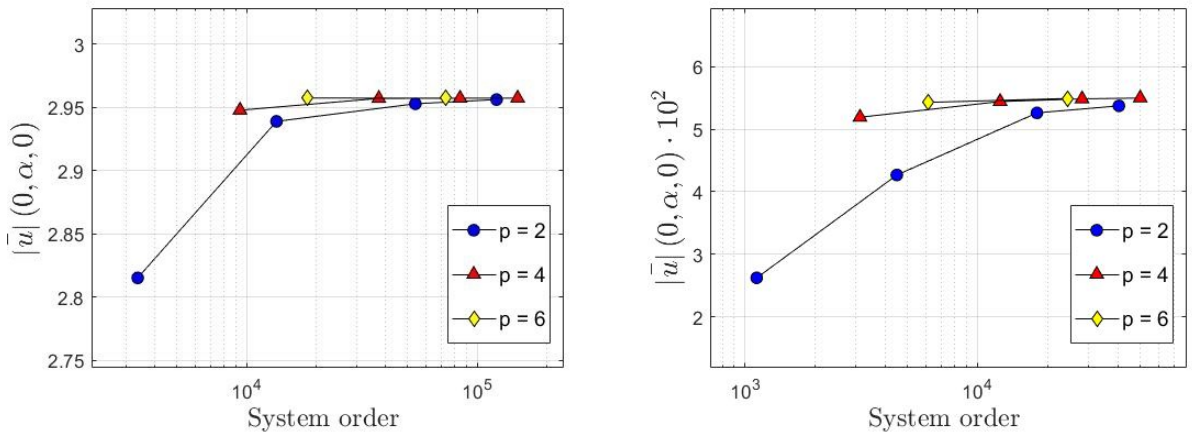

(a) (b)

Figure 6: Comparison between the convergence of the solution obtained by the present formulation for different polynomials orders p for the fuselage panel.

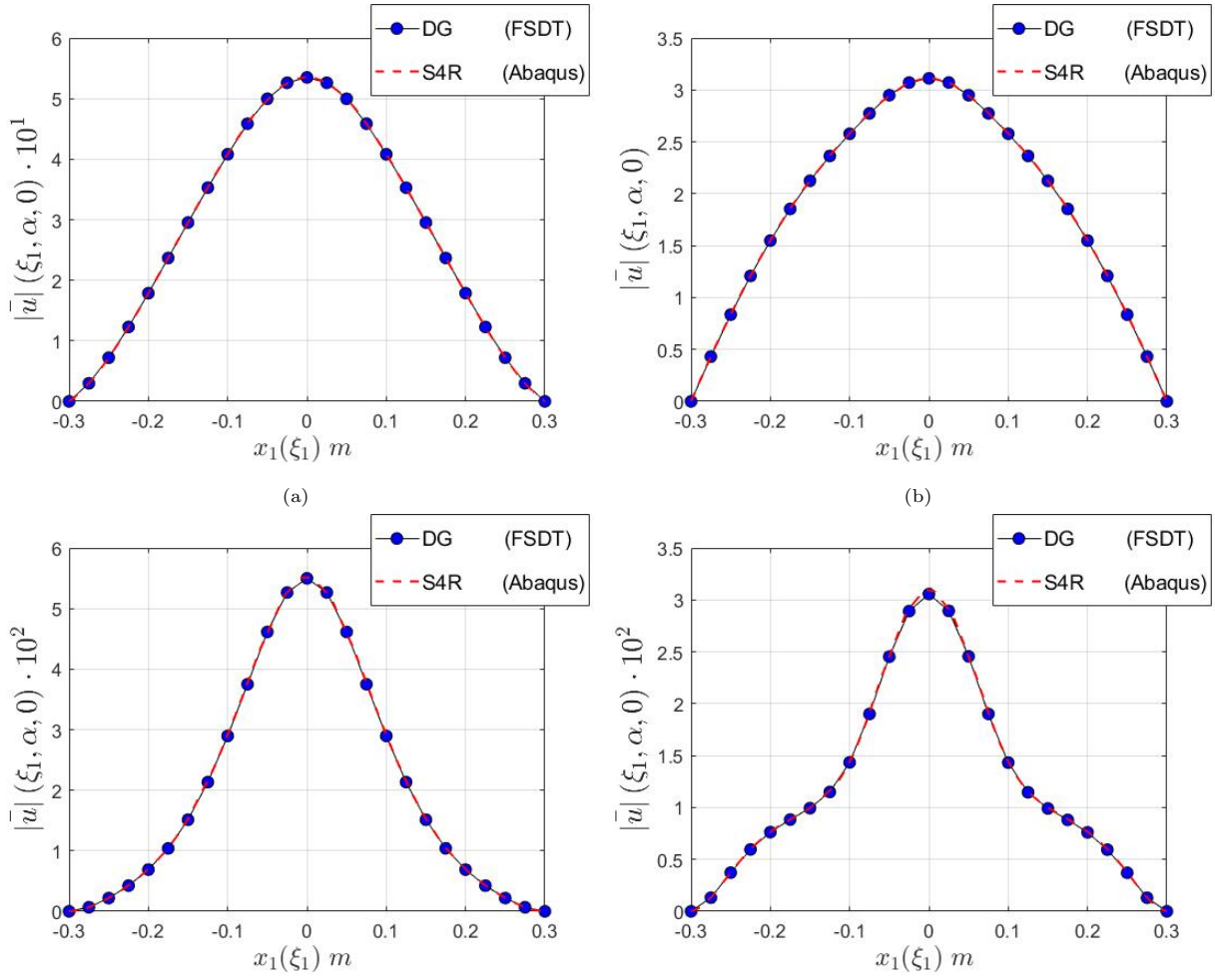

(a) (b) (c) (d)

Figure 7: Comparison between the FEM solution and the solution obtained by the present formulation for the fuselage panel.

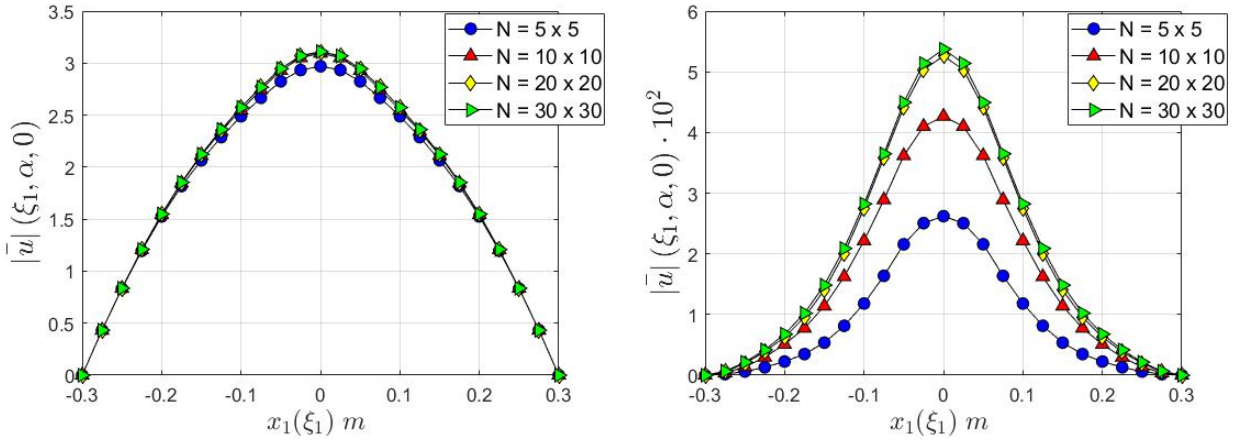

(a) (b)

Figure 8: Comparison between the solution obtained by the present formulation for different numbers of mesh elements for the fuselage panel.

5.2. Generally-curved NURBS-based shell

The second investigated geometry is defined in terms of NURBS functions as described by Eq.(5) where $\xi_1 \in [0, 1]$ and $\xi_2 \in [0, 1]$, the control points $\boldsymbol{P}_{ij}$ and their weights are given in Appendix Appendix B, and S_{ij} are the rational surface basis functions defined by the open knot vector $\{0, 0, 0, 0, 0, 0.2, 0.4, 0.6, 0.8, 1, 1, 1, 1, 1\}$ for both ξ_1 and ξ_2. It is noted that in this case the shell is represented by non-orthogonal curvilinear coordinates. The cut-out is obtained through the level set

$$\phi(\boldsymbol{x}_0) = a_n^{d_n} - |x_{01} - x_{1n}|^{d_n} - |x_{02} - x_{2n}|^{d_n}\,, \tag{37}$$

where a_n, d_n, x_{1n} and x_{2n} are reported in Tab.(1). The resulting shell geometry is displayed in Fig.(10). The shell is subjected to clamped boundary conditions on its lateral surfaces and traction free boundary conditions along the cut-out boundary, while a uniform pressure $\boldsymbol{t} = q_n \boldsymbol{g}^3$ is applied on the bottom surface.

The two shell sections labelled as N_1 and N_2 in Tab.(2) are investigated. The accuracy of the proposed method is assessed by comparing the solution computed with the present approach using the FSDT theory and a dG scheme with polynomial order $p = 6$ and the solution computed using Abaqus S3R shell elements. The comparison is shown in Fig.(11) in terms of the non-dimensional displacement magnitude defined as

$$|\overline{u}| \equiv |u| \cdot \left(\frac{\tau_n^3 E_r}{(L_n/2)^4 q_n} \right). \tag{38}$$

The value of $|\overline{u}|$ is computed along the curve identified by the points $\boldsymbol{x} = \boldsymbol{x}(\beta, \xi_2, 0)$ and along the curve identified by the points $\boldsymbol{x} = \boldsymbol{x}(\xi_1, \alpha, 0)$, where $\beta = 0.43$ and $\alpha = 0.55$. The former curve is indicated as s in Fig.(10c), while the latter is indicated as t in Fig.(10c). Figures (11a) and (11c) refer to the shell section N_1, while Figs.(11b) and (11d) refer to the shell section N_2. The obtained results confirm the accuracy of the proposed method also for a shell described by NURBS functions.

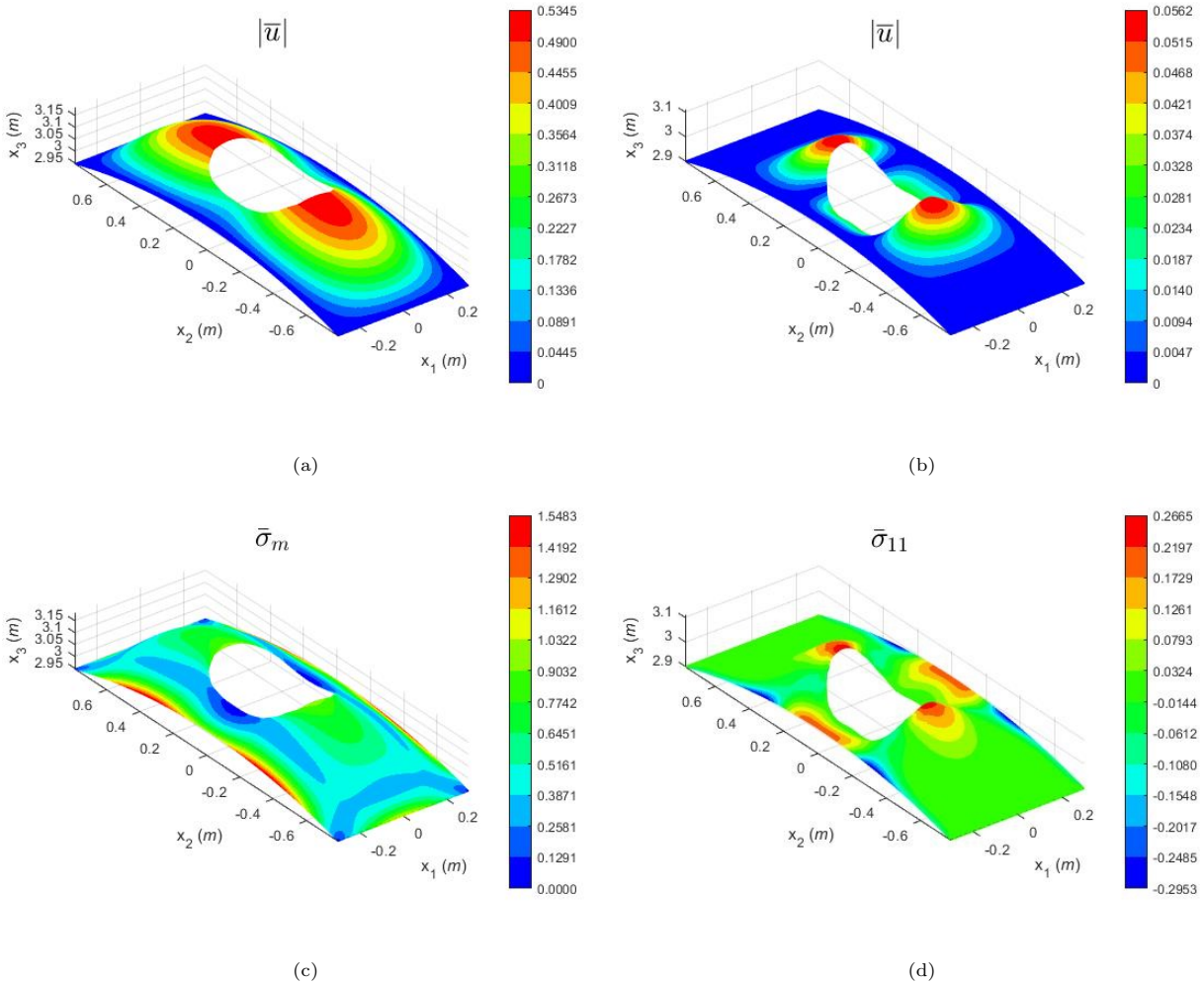

Figure 9: Deformed shape of the fuselage panel with superimposed contours of (a) the magnitude of the displacement and (c) the Von Mises stress for the section F_1, and (b) the magnitude of the displacement and (d) the stress component $\overline{\sigma}_{11}$ for the section F_3.

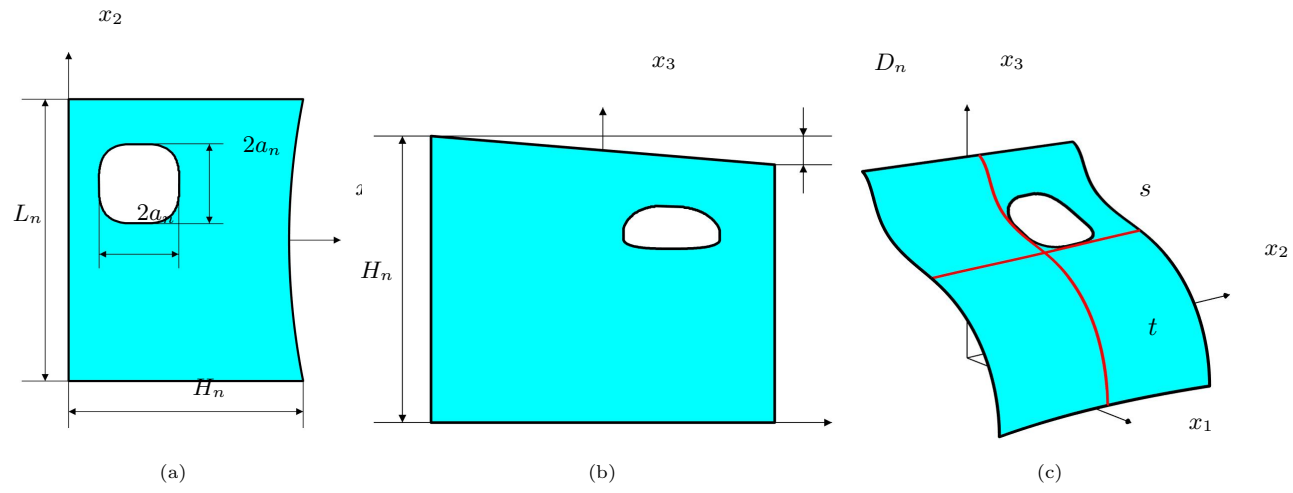

Figure 10: Geometry of the NURBS-based shell in three different views.

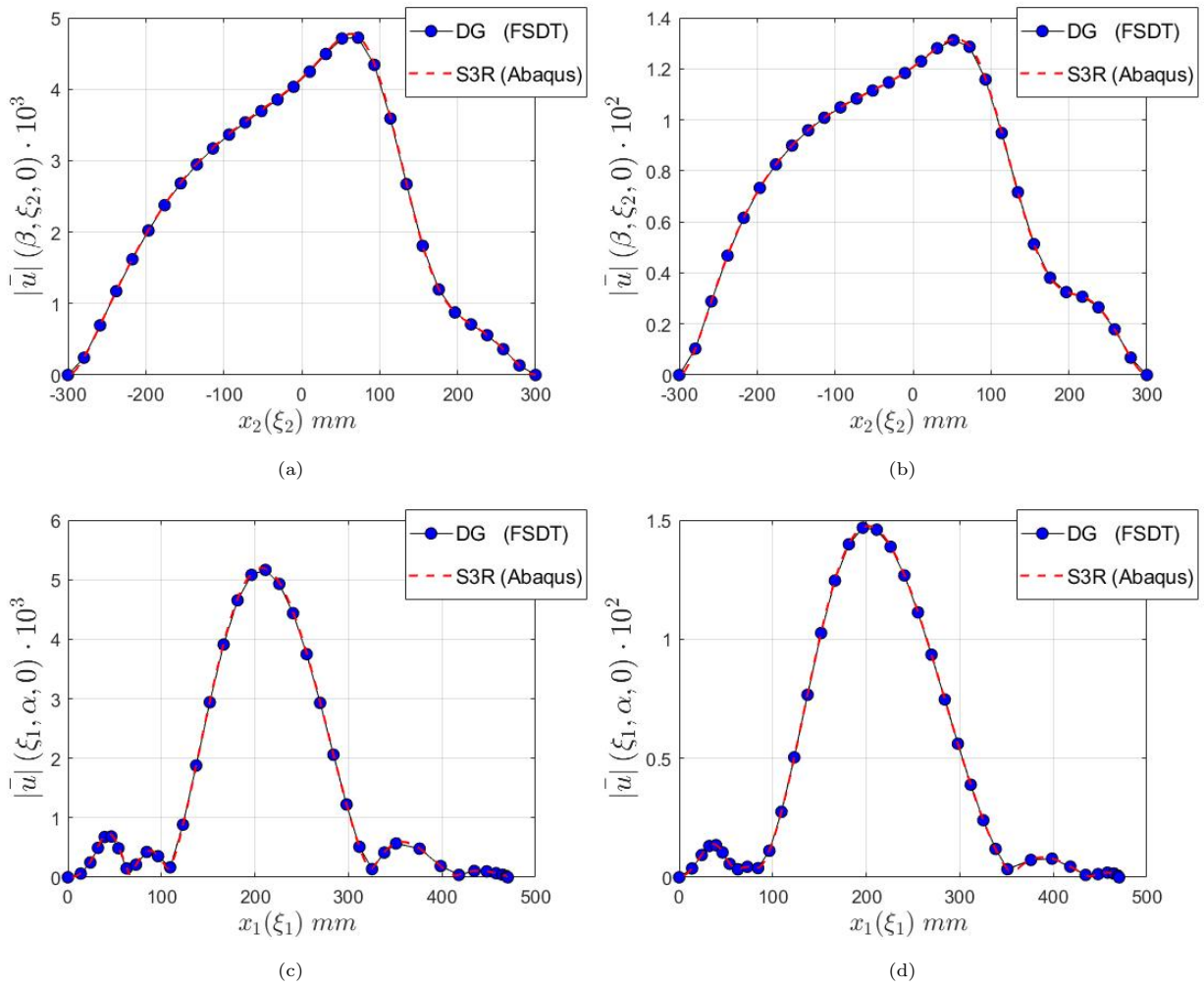

Figure 11: Comparison between the FEM solution and the solution obtained by the present formulation for the NURBS-based shell.

The effect of the mesh size on the value of $|\overline{u}|$ evaluated along the same curves using the FSDT theory and a dG scheme with polynomial order $p = 2$ is presented in Figs.(12a) and (12c) for the shell section N_1 and in Figs.(12b) and (12d) for the shell section N_2. The same convergence behavior is observed for the considered shell sections.

To conclude, Fig.(13) shows the deformed shape of the top surface of the considered shells with superimposed contour plots of the non-dimensional magnitude as given in Eq.(38) and two selected stress measures, which are evaluated using the following non-dimensional stress components

$$\overline{\sigma}_{ij} \equiv \sigma_{ij} \cdot \left(\frac{\tau_n^2}{(L_n/2)^2 q_n} \right). \tag{39}$$

The reported figures show the complex stress distribution induced by the interaction between the curvature of the shell and the presence of the cut-out.

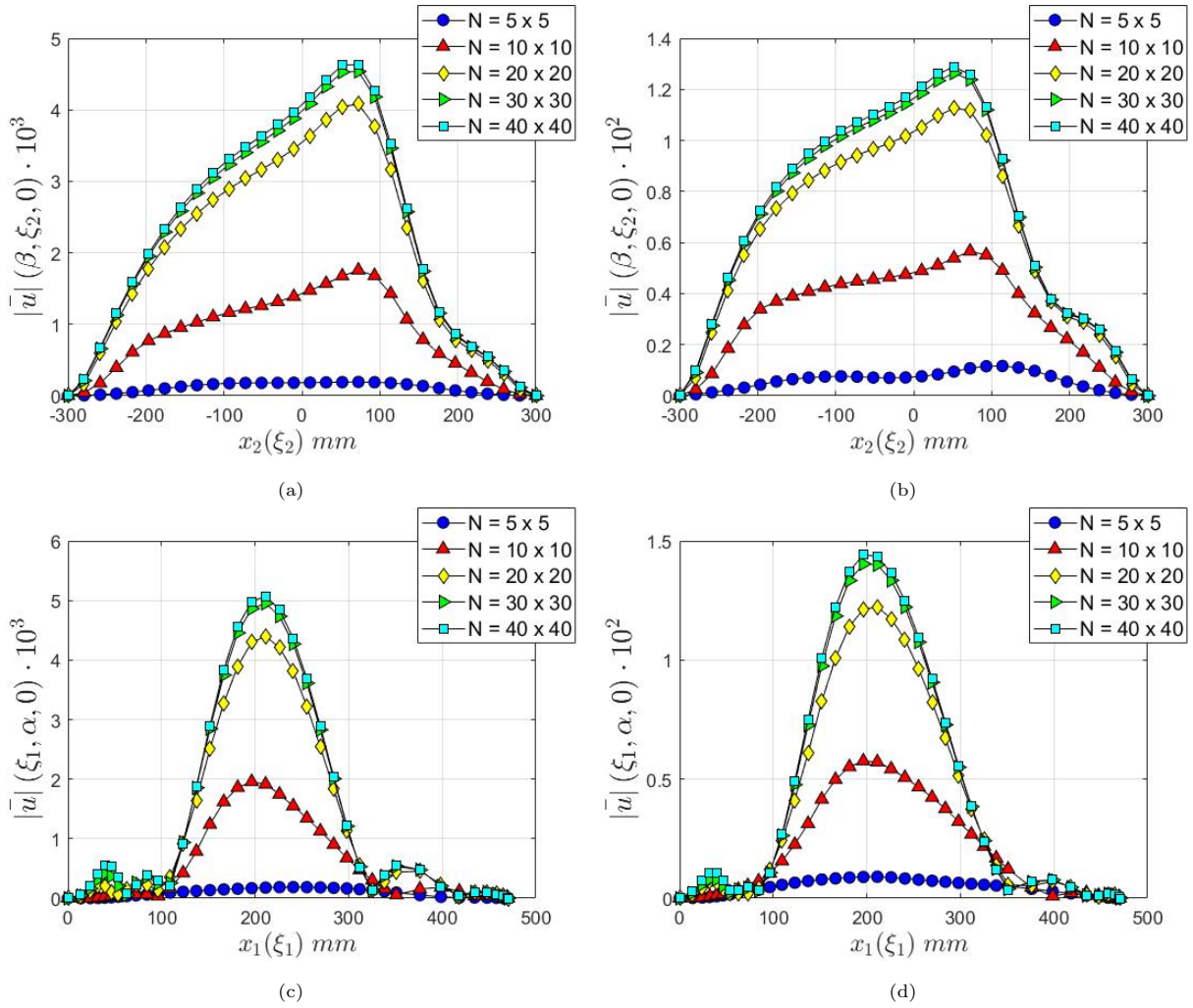

Figure 12: Comparison between the solution obtained by the present formulation for different numbers of mesh elements for the NURBS-based shell.

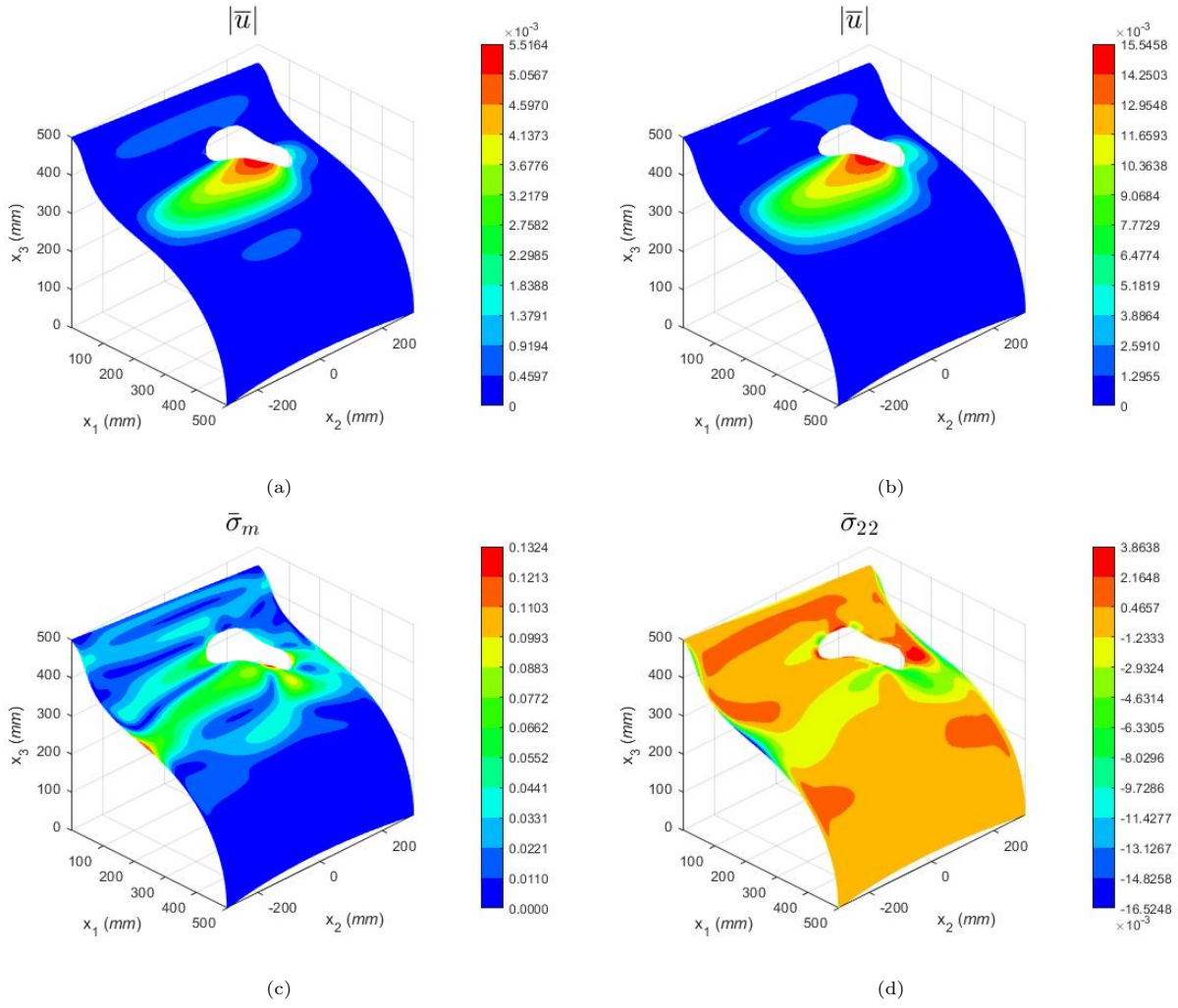

Figure 13: Deformed shape of the NURBS-based shell with superimposed contours of (a) the magnitude of the displacement and (c) the Von Mises stress for the section N_1, and (b) the magnitude of the displacement and (d) the stress component $\overline{\sigma}_{22}$ for the section N_2.

6. Conclusions

A novel high-fidelity numerical scheme for the static analysis of multilayered shells with cut-outs has been presented. The novel feature of the proposed scheme is the combined use of: *i*) an accurate representation of the shell geometry via either user-defined analytic functions or NURBS parametrizations, which can be imported from modern CAD libraries; *ii*) a flexible implicit representation of the embedded cut-outs via a level set function; *iii*) an ESL approach based on the expansion of the covariant components of the displacement field throughout the shell thickness, which allows considering in a unified fashion multiple higher-order shell theories, including the classic FSDT; *iv*) the implicitly-defined mesh technique, whereby the shell reference domain is discretized by intersecting an easy-to-generate background grid and the implicit representation of the cut-outs; *v*) an Interior Penalty discontinuous Galerkin method, which allows resolving with high-order accuracy the governing equations of the selected shell theory even in proximity of the embedded cut-outs thanks to the use of high-order quadrature rules for implicitly-defined domains and boundaries. The above features are tunable to obtain a high-order accurate treatment of the shell problem in terms of both the representation of the shell geometry and the resolution of the mechanical fields. This motivates the term high-fidelity.

To show the capabilities of the proposed scheme, a set of numerical tests involving the static response of two multilayered shell geometries with a cut-out was performed and discussed. The first group of tests geometry were focused on a cylindrical shell with a cut-out inspired by the geometry of fuselage panel with a windows. The second group of tests geometry were focused on a generally-curved NURBS-based shell where the level set function was chosen to represent an inspection door in the shell. Different shell sections, including a homogeneous isotropic shell, a homogeneous orthotropic shell and various multilayered shells, were tested. Several numerical tests were investigated and reported to show the effect of the mesh size and the polynomial order on the computed solution. The obtained results were also compared with the results obtained using the FEM library Abaqus. In all the considered tests cases, the proposed approach was able to reproduce accurately the FEM results. Moreover, by solving the same shell problem using the FSDT, a high-order shell theory and a 3D FEM model, it was shown that the high-order shell theory provides a more accurate solution than the low-order FSDT when both theories are compared to a fully 3D scheme.

Data availability statement

The data required to reproduce these findings cannot be shared at this time as they also form part of an ongoing study.

Acknowledgements

G.G. and A.M. acknowledge the support of the Italian Ministry of Education, University and Research – MIUR – through the project DEVISU, funded under the scheme PRIN-2107 – Grant 22017ZX9X4K 006.

Appendix A. Derivatives of the contravariant basis

The present formulation requires the knowledge of the matrix $\boldsymbol{R}$, whose columns are the vectors $\boldsymbol{g}^i$ of the contravariant basis, and its derivatives with respect to the curvilinear variables ξ_1 and ξ_2. For example, $\boldsymbol{R}$ and $\partial\boldsymbol{R}/\partial\xi_i$ enter the definitions of the matrices $\boldsymbol{J}_\alpha$ and $\boldsymbol{J}_0$ given in Eq.(19). However, despite the apparently complex expressions, to obtain $\boldsymbol{R}$ and $\partial\boldsymbol{R}/\partial\xi_i$, one needs only the derivatives of the shell mid-surface map as given in Eq.(1) with respect to ξ_1 and ξ_2 up to the third order. The aim of this appendix is then to provide a set of easy-to-use formulas to compute the quantities of interest for the present formulation.

Let us introduce the derivatives of the map given in Eq.(1) with respect to ξ_1 and ξ_2. Besides $\boldsymbol{a}_1$ and $\boldsymbol{a}_2$ defined in Eq.(2), ones has

$$\boldsymbol{a}_{11} \equiv \frac{\partial^2 \boldsymbol{x}_0}{\partial \xi_1^2}, \quad \boldsymbol{a}_{12} \equiv \frac{\partial^2 \boldsymbol{x}_0}{\partial \xi_1 \xi_2}, \quad \text{and} \quad \boldsymbol{a}_{22} \equiv \frac{\partial^2 \boldsymbol{x}_0}{\partial \xi_2^2}, \tag{A.1}$$

and

$$\boldsymbol{a}_{111} \equiv \frac{\partial^3 \boldsymbol{x}_0}{\partial \xi_1^3}, \quad \boldsymbol{a}_{112} \equiv \frac{\partial^3 \boldsymbol{x}_0}{\partial \xi_1^2 \xi_2}, \quad \boldsymbol{a}_{122} \equiv \frac{\partial^3 \boldsymbol{x}_0}{\partial \xi_1 \xi_2^2}, \quad \text{and} \quad \boldsymbol{a}_{222} \equiv \frac{\partial^3 \boldsymbol{x}_0}{\partial \xi_2^3}. \tag{A.2}$$

The derivatives of the vector $\boldsymbol{a}_3$ defined in Eq.(2) are easily computed as follows

$$\frac{\partial \boldsymbol{a}_3}{\partial \xi_1} = \boldsymbol{a}_{11} \times \boldsymbol{a}_2 + \boldsymbol{a}_1 \times \boldsymbol{a}_{12}, \tag{A.3a}$$

$$\frac{\partial \boldsymbol{a}_3}{\partial \xi_2} = \boldsymbol{a}_{12} \times \boldsymbol{a}_2 + \boldsymbol{a}_1 \times \boldsymbol{a}_{22}, \tag{A.3b}$$

$$\frac{\partial^2 \boldsymbol{a}_3}{\partial \xi_1^2} = \boldsymbol{a}_{111} \times \boldsymbol{a}_2 + 2\ \boldsymbol{a}_{11} \times \boldsymbol{a}_{12} + \boldsymbol{a}_1 \times \boldsymbol{a}_{112}, \tag{A.3c}$$

$$\frac{\partial^2 \boldsymbol{a}_3}{\partial \xi_1 \xi_2} = \boldsymbol{a}_{112} \times \boldsymbol{a}_2 + \boldsymbol{a}_{11} \times \boldsymbol{a}_{22} + \boldsymbol{a}_{12} \times \boldsymbol{a}_{12} + \boldsymbol{a}_1 \times \boldsymbol{a}_{122}, \tag{A.3d}$$

$$\frac{\partial^2 \boldsymbol{a}_3}{\partial \xi_2^2} = \boldsymbol{a}_{122} \times \boldsymbol{a}_2 + 2\ \boldsymbol{a}_{12} \times \boldsymbol{a}_{22} + \boldsymbol{a}_1 \times \boldsymbol{a}_{222}. \tag{A.3e}$$

Let us now introduce the scalar λ and the matrix $\boldsymbol{M}$ as

$$\lambda \equiv ||\boldsymbol{a}_3|| \quad \text{and} \quad \boldsymbol{M} \equiv \frac{1}{\lambda}(\boldsymbol{I} - \boldsymbol{n}_0 \boldsymbol{n}_0^\intercal) \tag{A.4}$$

where $\boldsymbol{n}_0$ is defined in Eq.(2) and $\boldsymbol{I}$ is the 3×3 identity matrix. The derivatives of the unit normal $\boldsymbol{n}_0$ are then computed in terms of the derivatives of $\boldsymbol{a}_3$ as

$$\frac{\partial \boldsymbol{n}_0}{\partial \xi_\alpha} = \boldsymbol{M} \frac{\partial \boldsymbol{a}_3}{\partial \xi_\alpha}, \tag{A.5a}$$

$$\frac{\partial^2 \boldsymbol{n}_0}{\partial \xi_\alpha \xi_\beta} = \boldsymbol{M} \frac{\partial^2 \boldsymbol{a}_3}{\partial \xi_\alpha \xi_\beta} - \frac{1}{\lambda} \left(\boldsymbol{M} \left(\boldsymbol{n}_0^\intercal \frac{\partial \boldsymbol{a}_3}{\partial \xi_\beta} \right) + \boldsymbol{M} \frac{\partial \boldsymbol{a}_3}{\partial \xi_\beta} \boldsymbol{n}_0^\intercal + \boldsymbol{n}_0 \frac{\partial \boldsymbol{a}_3^\intercal}{\partial \xi_\beta} \boldsymbol{M} \right) \frac{\partial \boldsymbol{a}_3}{\partial \xi_\alpha}, \tag{A.5b}$$

Finally, upon introducing the matrix $\boldsymbol{P}$, whose columns are the vectors $\boldsymbol{g}_i$ of the covariant basis, i.e.

$$\boldsymbol{P} \equiv \left[\begin{array}{ccc} \boldsymbol{g}_1 & \boldsymbol{g}_2 & \boldsymbol{g}_3 \end{array} \right] = \left[\begin{array}{ccc} \boldsymbol{a}_1 + \xi_3 \frac{\partial \boldsymbol{n}_0}{\partial \xi_1} & \boldsymbol{a}_2 + \xi_3 \frac{\partial \boldsymbol{n}_0}{\partial \xi_2} & \boldsymbol{n}_0 \end{array} \right], \tag{A.6}$$

one has

$$\begin{aligned}
\frac{\partial \boldsymbol{P}}{\partial \xi_1} &\equiv \left[\begin{array}{ccc} \boldsymbol{a}_{11} + \xi_3 \frac{\partial^2 \boldsymbol{n}_0}{\partial \xi_1^2} & \boldsymbol{a}_{12} + \xi_3 \frac{\partial^2 \boldsymbol{n}_0}{\partial \xi_1 \xi_2} & \frac{\partial \boldsymbol{n}_0}{\partial \xi_1} \end{array} \right] \\
\frac{\partial \boldsymbol{P}}{\partial \xi_2} &\equiv \left[\begin{array}{ccc} \boldsymbol{a}_{12} + \xi_3 \frac{\partial^2 \boldsymbol{n}_0}{\partial \xi_1 \xi_2} & \boldsymbol{a}_{22} + \xi_3 \frac{\partial^2 \boldsymbol{n}_0}{\partial \xi_2^2} & \frac{\partial \boldsymbol{n}_0}{\partial \xi_2} \end{array} \right] \\
\frac{\partial \boldsymbol{P}}{\partial \xi_3} &\equiv \left[\begin{array}{ccc} \frac{\partial \boldsymbol{n}_0}{\partial \xi_1} & \frac{\partial \boldsymbol{n}_0}{\partial \xi_2} & \boldsymbol{0} \end{array} \right]
\end{aligned} \tag{A.7}$$

and

$$\frac{\partial \boldsymbol{R}}{\partial \xi_i} = -\boldsymbol{R} \frac{\partial \boldsymbol{P}^{\intercal}}{\partial \xi_i} \boldsymbol{R}, \tag{A.8}$$

where Eq.(A.8) is obtained by using $\boldsymbol{R} = \boldsymbol{P}^{-\intercal}$ [32].

As a last comment, it is worth reporting that the derivatives of the shell mid-surface map described by user-defined analytical functions were computed using the Python [39] library *sympy* [40] for symbolic calculus, whereas the derivatives of the NURBS-based parametrizations were evaluated using the algorithms described by Piegl and Tiller [34] and available in the library *geomdl* [41].

Appendix B. Control Points

For the sake of completeness, the control points used in the definition of the mid-surface of the NURBS-based shell shown in Fig.(10) are listed in Tab.(B.4). For each control point it is reported the correspondent indices i and j, the coordinates x_1, x_2 and x_3 in mm and the weight h_{ij}.

Table B.4: List of control points for the NURBS surface in Fig.(10).

i,j	x_1	x_2	x_3	h_{ij}	i,j	x_1	x_2	x_3	h_{ij}	i,j	x_1	x_2	x_3	h_{ij}
1,1	0.00	-300.00	500.00	1	4,1	153.89	-300.00	328.89	1	7,1	489.97	-300.00	108.82	1
1,2	0.00	-270.00	497.49	1	4,2	152.46	-270.00	327.10	1	7,2	484.12	-270.00	108.82	1
1,3	0.00	-210.00	492.48	1	4,3	150.54	-210.00	323.51	1	7,3	474.05	-210.00	108.83	1
1,4	0.00	-120.00	484.99	1	4,4	149.50	-120.00	318.55	1	7,4	463.69	-120.00	108.84	1
1,5	0.00	0.00	475.01	1	4,5	148.91	0.00	314.01	1	7,5	459.16	0.00	108.85	1
1,6	0.00	120.00	465.04	1	4,6	145.18	120.00	313.29	1	7,6	463.69	120.00	108.83	1
1,7	0.00	210.00	457.53	1	4,7	142.95	210.00	314.32	1	7,7	474.05	210.00	108.82	1
1,8	0.00	270.00	452.51	1	4,8	142.70	270.00	315.27	1	7,8	484.15	270.00	108.81	1
1,9	0.00	300.00	450.00	1	4,9	143.04	300.00	315.74	1	7,9	490.01	300.00	108.80	1
2,1	36.11	-300.00	483.13	1	5,1	304.62	-300.00	309.21	1	8,1	500.01	-300.00	36.28	1
2,2	36.06	-270.00	480.98	1	5,2	301.48	-270.00	308.51	1	8,2	493.99	-270.00	36.28	1
2,3	36.00	-210.00	476.67	1	5,3	296.52	-210.00	307.12	1	8,3	483.58	-210.00	36.28	1
2,4	36.01	-120.00	470.21	1	5,4	292.27	-120.00	305.19	1	8,4	472.81	-120.00	36.27	1
2,5	36.10	0.00	461.57	1	5,5	290.80	0.00	303.39	1	8,5	468.02	0.00	36.27	1
2,6	36.10	120.00	452.86	1	5,6	290.63	120.00	303.04	1	8,6	472.78	120.00	36.28	1
2,7	36.16	210.00	446.27	1	5,7	293.65	210.00	303.37	1	8,7	483.54	210.00	36.28	1
2,8	36.26	270.00	441.86	1	5,8	297.79	270.00	303.69	1	8,8	493.97	270.00	36.28	1
2,9	36.33	300.00	439.65	1	5,9	300.52	300.00	303.85	1	8,9	500.00	300.00	36.28	1
3,1	41.45	-300.00	387.42	1	6,1	441.80	-300.00	213.61	1	9,1	500.00	-300.00	0.00	1
3,2	41.14	-270.00	385.76	1	6,2	436.77	-270.00	213.52	1	9,2	493.98	-270.00	0.00	1
3,3	40.80	-210.00	382.44	1	6,3	428.27	-210.00	213.33	1	9,3	483.57	-210.00	0.00	1
3,4	40.79	-120.00	377.66	1	6,4	419.88	-120.00	213.07	1	9,4	472.80	-120.00	0.00	1
3,5	40.62	0.00	372.26	1	6,5	416.46	0.00	212.86	1	9,5	468.01	0.00	0.00	1
3,6	38.78	120.00	368.63	1	6,6	419.60	120.00	212.87	1	9,6	472.77	120.00	0.00	1
3,7	37.28	210.00	366.62	1	6,7	427.79	210.00	212.98	1	9,7	483.54	210.00	0.00	1
3,8	36.60	270.00	365.41	1	6,8	436.17	270.00	213.06	1	9,8	493.97	270.00	0.00	1
3,9	36.40	300.00	364.80	1	6,9	441.15	300.00	213.10	1	9,9	500.00	300.00	0.00	1

References

[1] R. Jones, Mechanics Of Composite Materials, Materials Science and Engineering Series, Taylor & Francis, 1998.

[2] J. Reddy, Theory and Analysis of Elastic Plates and Shells, Series in Systems and Control, CRC Press, 2006.

[3] J. Reddy, C. Liu, A higher-order shear deformation theory of laminated elastic shells, International journal of engineering science 23 (3) (1985) 319–330.

[4] M. Cho, K.-O. Kim, M.-H. Kim, Efficient higher-order shell theory for laminated composites, Composite Structures 34 (2) (1996) 197–212.

[5] E. Viola, F. Tornabene, N. Fantuzzi, General higher-order shear deformation theories for the free vibration analysis of completely doubly-curved laminated shells and panels, Composite Structures 95 (2013) 639–666.

[6] E. Carrera, Mixed layer-wise models for multilayered plates analysis, Composite Structures 43 (1) (1998) 57–70.

[7] J. N. Reddy, M. Savoia, Layer-wise shell theory for postbuckling of laminated circular cylindrical shells, AIAA Journal 30 (8) (1992) 2148–2154.

[8] M. Epstein, H.-P. Huttelmaier, A finite element formulation for multilayered and thick plates, Computers & Structures 16 (5) (1983) 645–650.

[9] E. Carrera, Theories and finite elements for multilayered plates and shells: a unified compact formulation with numerical assessment and benchmarking, Archives of Computational Methods in Engineering 10 (3) (2003) 215–296.

[10] E. Carrera, Introduction to the Unified Formulation, Wiley, 2014, Ch. 5, pp. 51–69.

[11] A. S. Sayyad, Y. M. Ghugal, Static and free vibration analysis of laminated composite and sandwich spherical shells using a generalized higher-order shell theory, Composite Structures 219 (2019) 129–146.

[12] D. An, D. Xu, Z. Ni, Y. Su, B. Wang, R. Li, Finite integral transform method for analytical solutions of static problems of cylindrical shell panels, European Journal of Mechanics - A/Solids 83 (2020) 104033.

[13] P. Kumari, S. Kar, Static behavior of arbitrarily supported composite laminated cylindrical shell panels: An analytical 3d elasticity approach, Composite Structures 207 (2019) 949–965.

[14] G. M. Kulikov, S. V. Plotnikova, Exact geometry four-node solid-shell element for stress analysis of functionally graded shell structures via advanced sas formulation, Mechanics of Advanced Materials and Structures 27 (12) (2020) 948–964.

[15] A. Madeo, F. S. Liguori, G. Zucco, S. Fiore, An efficient isostatic mixed shell element for coarse mesh solution, International Journal for Numerical Methods in Engineering 122 (1) (2021) 82–121.

[16] F. Tornabene, N. Fantuzzi, E. Viola, E. Carrera, Static analysis of doubly-curved anisotropic shells and panels using cuf approach, differential geometry and differential quadrature method, Composite Structures 107 (2014) 675–697.

[17] F. Tornabene, M. Viscoti, R. Dimitri, M. A. Aiello, Higher order formulations for doubly-curved shell structures with a honeycomb core, Thin-Walled Structures 164 (2021) 107789.

[18] A. Milazzo, V. Oliveri, Post-buckling analysis of cracked multilayered composite plates by pb-2 rayleigh–ritz method, Composite Structures 132 (2015) 75–86.

[19] V. Gulizzi, V. Oliveri, A. Milazzo, Buckling and post-buckling analysis of cracked stiffened panels via an x-ritz method, Aerospace Science and Technology 86 (2019) 268–282.

[20] G. Sciascia, V. Oliveri, A. Milazzo, P. M. Weaver, Ritz solution for transient analysis of variable-stiffness shell structures, AIAA Journal 58 (4) (2020) 1796–1810.

[21] T. Hughes, J. Cottrell, Y. Bazilevs, Isogeometric analysis: Cad, finite elements, nurbs, exact geometry and mesh refinement, Computer Methods in Applied Mechanics and Engineering 194 (39) (2005) 4135–4195.

[22] D. N. Arnold, F. Brezzi, Cockburn, B., L. D. Marini, Unified analysis of discontinuous galerkin methods for elliptic problems, SIAM journal on numerical analysis 39 (5) (2002) 1749–1779.

[23] B. Rivière, S. Shaw, M. F. Wheeler, J. Whiteman, Discontinuous galerkin finite element methods for linear elasticity and quasistatic linear viscoelasticity, Numerische Mathematik 95 (2003) 347–376.

[24] A. Ten Eyck, A. Lew, Discontinuous galerkin methods for non-linear elasticity, International Journal for Numerical Methods in Engineering 67 (9) (2006) 1204–1243.

[25] L. Noels, R. Radovitzky, A new discontinuous galerkin method for kirchhoff–love shells, Computer Methods in Applied Mechanics and Engineering 197 (33-40) (2008) 2901–2929.

[26] B. L. Talamini, R. Radovitzky, A discontinuous galerkin method for nonlinear shear-flexible shells, Computer methods in applied mechanics and engineering 303 (2016) 128–162.

[27] P. R. Bösing, A. L. Madureira, I. Mozolevski, A new interior penalty discontinuous galerkin method for the reissner–mindlin model, Mathematical Models and Methods in Applied Sciences 20 (08) (2010) 1343–1361.

[28] V. Gulizzi, I. Benedetti, A. Milazzo, An implicit mesh discontinuous galerkin formulation for higher-order plate theories, Mechanics of Advanced Materials and Structures 27 (17) (2020) 1494–1508.

[29] V. Gulizzi, I. Benedetti, A. Milazzo, A high-resolution layer-wise discontinuous galerkin formulation for multilayered composite plates, Composite Structures (2020) 112137.

[30] I. Benedetti, V. Gulizzi, A. Milazzo, Layer-wise discontinuous galerkin methods for piezoelectric laminates, Modelling 1 (2) (2020) 198–214.

[31] G. Guarino, A. Milazzo, V. Gulizzi, Equivalent-single-layer discontinuous galerkin methods for static analysis of multilayered shells, Applied Mathematical Modelling 98 (2021) 701–721.

[32] P. G. Ciarlet, An introduction to differential geometry with applications to elasticity, Journal of Elasticity 78 (1-3) (2005) 1–215.

[33] D. F. Rogers, An Introduction to NURBS: With Historical Perspective, Morgan Kaufmann Publishers Inc., 2001.

[34] L. Piegl, W. Tiller, The NURBS Book (monographs in visual communication), Springer, 1997.

[35] T. Ting, Anisotropic Elasticity: Theory and Applications, Oxford Engineering Science Series.

[36] E. Carrera, Theories and finite elements for multilayered, anisotropic, composite plates and shells, Archives of Computational Methods in Engineering 9 (2) (2002) 87–140.

[37] R. I. Saye, High-order quadrature methods for implicitly defined surfaces and volumes in hyperrectangles, SIAM Journal on Scientific Computing 37 (2) (2015) A993–A1019.

[38] M. Smith, ABAQUS 6.14 Documentation, Dassault Systèmes, 2014, providence, RI, USA.

[39] G. Van Rossum, F. L. Drake Jr, Python tutorial, Centrum voor Wiskunde en Informatica Amsterdam, The Netherlands, 1995.

[40] A. Meurer, C. Smith, M. Paprocki, O. Čertík, S. Kirpichev, M. Rocklin, A. Kumar, S. Ivanov, J. Moore, S. Singh, T. Rathnayake, S. Vig, B. Granger, R. Muller, F. Bonazzi, H. Gupta, S. Vats, F. Johansson, F. Pedregosa, A. Scopatz, Sympy: Symbolic computing in python, PeerJ Computer Science 3 (2017) e103.

[41] O. R. Bingol, A. Krishnamurthy, Nurbs-python: An open-source object-oriented nurbs modeling framework in python, SoftwareX 9 (2019) 85–94.